Viscoelastic relaxation: A mechanism to explain the decennial large surface displacements at the Laguna del Maule silicic volcanic complex

Camila Novoa, Denise Rémy, Muriel Gerbault, Juan C. Baez, Andrés Tassara, Loreto Cordova, Carlos Cardona, M. Granger, Sylvain Bonvalot, Francisco Delgado

Viscoelastic relaxation: A mechanism to explain the decennial large surface displacements at the Laguna del Maule silicic volcanic complex

C. Novoa [a,b,*], D. Remy [a], M. Gerbault [a], J.C. Baez [c], A. Tassara [d], L. Cordova [e], C. Cardona [e], M. Granger [a], S. Bonvalot [a], F. Delgado [f]

[a] GET/UMR5563 (UPS, CNRS, IRD, CNES); Obs. Midi-Pyrénées, Université P. Sabatier, Toulouse, France
[b] Programa Doctorado en Ciencias Geologicas, Facultad de Ciencias Químicas, Universidad de Concepción, Chile
[c] Centro Sismológico Nacional, Universidad de Chile, Santiago, Chile
[d] Departamento Ciencias de la Tierra, Facultad de Ciencias Químicas, Universidad de Concepción, Victor Lamas 1290, Concepcion, Chile
[e] Observatorio Volcanológico Chileno, Servicio Nacional de Geología y Mineria, Rudecindo Ortega 03850, Temuco, Chile
[f] Institut de Physique du Globe de Paris, Sorbonne Paris Cité, Univ. Paris Diderot, UMR 7154 CNRS, Paris, France

ARTICLE

Keywords:
Andes Southern Volcanic Zone InSAR
GNSS
viscoelasticity
mush reservoir
volcanic unrest

ABSTRACT

Silicic systems generate the most explosive eruptions on Earth. In contrast to basaltic systems, they can accumulate large volumes of magma without systematically erupting, confronting the classical interpretation that a volcano inflates when a magmatic intrusion occurs. Understanding the mechanisms of volcanic inflation and unrest is thus one of the most important challenges in volcanic risk assessment. Laguna del Maule (LdM) in the Southern Volcanic Zone (SVZ) of Chile, is one of the most active Holocene silicic complexes in the world and it has been inflating since 2007, accumulating 2 m of uplift without erupting. Several geophysical and geochemical studies conclude that a large crystal rich reservoir would be residing beneath LdM, in consistency with other multi-disciplinary studies showing that such crystal-rich reservoirs ("mush zones") can be maintained beneath silicic volcanoes, fed by mafic magma recharge from below. Nevertheless, the mechanical state of such reservoirs remains unclear. Here, we characterize for the first time the mechanical properties of such a mush reservoir, able to promote large surface displacements such as those measured at LdM. Using a 3D finite element method we simulate a recharge of magma at the base of a crystal rich reservoir, by assuming an overpressurized source surrounded by a large viscoelastic shell. Inversion results show that this model fits the observed temporal and spatial evolution of ground displacements measured with InSAR data and GNSS data between 2007 and 2017. We interpret the temporal behavior of ground displacement at LdM as resulting from two contributions. A magma recharge occurred within the first 4 yr of the active inflation, followed by the viscous response of the large viscoelastic shell, set to a viscosity of 10^{17} Pas. Compared to a purely elastic solution, our model suggests that up to 50% of the accumulated surface displacement during the ten-year period can be explained by this viscous response, and predicts ongoing displacements 50 yr after the onset of inflation. This model agrees with geophysical and geochemical observations and offers a simple explanation of the temporal evolution of surface displacements. It further allows to reconsider the mechanical behavior of large partially crystallized domains in the upper crust; such significant transient stress transfer over large viscoelastic areas should thus be accounted for in other studies of silicic volcanic complexes.

1. Introduction

Silicic systems generate the most explosive eruptions on Earth. They can accumulate large volumes of rhyodacitic or rhyolitic magmas (Degruyter and Huber, 2014) and display sometimes large inflation signals over several years, without necessarily leading to an eruption. The origin of this unrest remains unclear and is subject of debate in many volcanic complexes such as Long Valley, Campi Flegrei, Yellowstone and many others (Pritchard et al., 2019). To improve eruptions forecasting, understanding the mechanical unrest of these silicic systems constitutes a fundamental question, if not one of the most important challenges in volcanology (Segall, 2019; Pritchard et al., 2019). Here, we study the unrest of Laguna del Maule over the last decade, but the mechanism that we propose may also explain the unrest of other silicic systems.

* Corresponding author at: GET/UMRS563 (UPS, CNRS, IRD, CNES); Obs. Midi-Pyrénées, Université P. Sabatier, Toulouse, France.
E-mail address: camila.novoa@get.omp.eu (C. Novoa).

https://doi.org/10.1016/j.epsl.2019.06.005

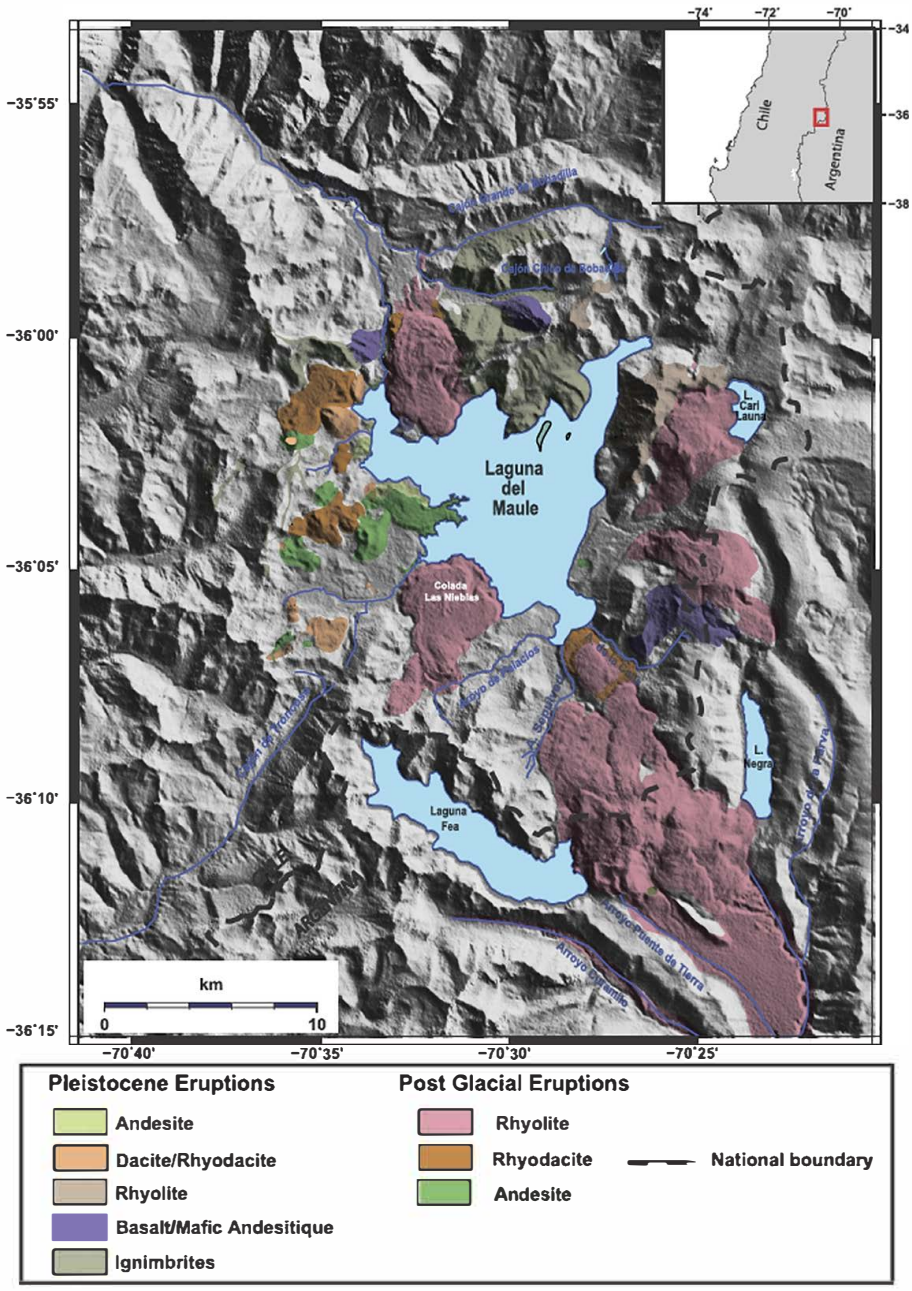

Fig. 1. Reference map of the study area in southern Chile corresponding to the black box in the right-hand inset map. A simplified geological map of the study area (after Hildreth et al., 2010 and Andersen et al., 2017) overlaid onto a shaded relief map, showing the emplacement of the main lava flows and their composition. (For interpretation of the colors in the figure(s), the reader is referred to the web version of this article.)

The Laguna del Maule (LdM) (Fig. 1) is a rhyolitic volcanic field located in the Southern Volcanic Zone (SVZ) of Chile that last erupted ~2000 yr ago (Andersen et al., 2012). It is considered to be an active rhyolitic complex since it displays the highest frequency of eruptions in the world (Hildreth et al., 2010) with a minimum of 50 rhyolitic eruptions in the last 26.000 yr. It is characterized by a ring of 36 post-glacial rhyolite and rhyodacite coulees and domes erupted from 24 silicic vents which are distributed over a wide basin of about 300 km^2. Lava flows from this highest concentration of silicic vents observed in the Southern Volcanic Zone covered an area of 100 km^2, for a total lava volume of about 6.4 km^3 (Hildreth et al., 2010).

The LdM volcanic field has fostered huge interest from the geodesy community in the last decade because it is one of the strongest deforming volcanic zone on Earth. Based on the analysis of Synthetic Aperture Radar (InSAR) data acquired between 2001 to 2008, Fournier et al. (2010) presented the first evidence of a strong inflation up to ~18 cm/yr over an elliptical area of 26 km NNE-SSW major axis and 19 km minor axis starting sometime between February 2004 and January 2007 (the lack of well-correlated interferograms spanning this period prevents precise determination of the displacement onset). Using InSAR and Global Navigation Satellite System (GNSS) data, Feigl et al. (2013) showed the persistence of this large-wavelength inflation and provided a value of the displacement rate observed at the center of the inflation of about 28 cm/yr for the 2007–2012 period. The studies carried out by Le Mével et al. (2015, 2016) revealed a temporal change in behavior of the displacement rate with 24 ± 0.6 cm/yr from 2007 to early 2010 decaying to 22 cm/yr in 2014 (consistent with a nearly linear temporal behavior after 2010).

Fournier et al. (2010), Feigl et al. (2013) and Le Mével et al. (2015) proposed that this uplift observed at LdM was caused by an inflating sill located at about 5 km depth. These studies assumed that the crust surrounding the displacement sources behaved as a pure elastic solid (Okada, 1985). Only Le Mével et al. (2016) considered a more complex viscoelastic response of the rocks in the vicinity of the pressurized source. These authors propose to explain the change in temporal behavior of surface displacements by viscous magma influx from a deep chamber into a shallow chamber connected by a vertical conduit. In this model the magma's influx asymptotically approaches zero as the pressure balance of this plumbing system is reached. It allows them to correlate the change in observed surface uplift rate with a bi-modal evolution of magma volume flow rate from 0.03 km^3/yr from 2007 to mid-2009 to 0.02 km^3/yr from mid-2009 to late 2014.

Multiple lines of evidence suggest the presence of a crystal rich reservoir at shallow crustal level beneath the LdM volcanic field. Field observations and geochemical data indicate that the huge concentration of silicic vents observed in the area is rather due to a large upper-crustal magma chamber evolving throughout postglacial times, instead of a deeper (*i.e.* 20 km) crustal melting zone releasing recurrent batches of ascending silicic magma (Hildreth et al., 2010). From geochemical analysis, Andersen et al. (2017) argued that all eruptions since 26 kyr were fed by the same large crystallized reservoir, despite differences between the northern and southern domains of the LdM. According to these authors, the crustal reservoir system would be thinner in the north leading to a lower residence time of the magmatic intrusion and inducing andesitic vent compositions, in contrast to the southern part of LdM where principally rhyolitic eruptions occurred. Magnetotelluric (MT) studies in turn (Singer et al., 2014; Wagner et al., 2017; Cordell et al., 2018) indicate the presence of a conductive body in the northern part of LdM at about 5 km depth, which was interpreted as a hot partially molten body. On the other hand, in the southern part of LdM, Bouguer gravity anomalies indicate an anomaly of −19 mGal centered below the observed on-going inflation (Nieblas area, Fig. 1), which would be caused by a low density mostly crystallized magma body (∼115 km^3) containing some 30 km^3 of crystal poor rhyolite magma (>85 % of melt) (Miller et al., 2017). Cordell et al. (2018) support the hypothesis of a large crystal rich reservoir beneath the observed on-going inflation, but question the existence of 30 km^3 of molten magma, arguing that it would then be detected by their magnetotelluric study (MT). From these different studies, it appears reasonable to consider that beneath the entire volcanic complex of LdM a large partially molten body may have been residing since at least the last 26 kyr, but both the geometry and the storage duration of this magma source remains unclear. Here we will investigate how such a hypothesis may help to interpret the strong surface displacements measured in the Nieblas area.

In this study, we benefit from a long InSAR time series of ground surface displacement at LdM spanning a period of ten years to analyze the characteristic of the surface displacement source and its time-dependent behavior. First, to constrain the geometry of the source, we invert the InSAR time series considering that surface displacements are triggered by an increase in internal pressure within a massive source assuming that the crust acts as a pure elastic medium. Next, in order to account for a more complex rheology related to the presence of a mush reservoir beneath LdM, we use a 3D finite element approach to study the viscoelastic response of a large crystal rich reservoir to an inflating basal magma source. We invert the InSAR and GNSS time series with this model to constrain the duration of the source's inflation and the viscosity associated to this crystal rich reservoir beneath LdM. The results show that both sets of elastic and visco-elastic models are able to explain the measured ground surface displacement at LdM. However they both lead to different conclusions, and provide useful information for a better characterization and understanding of the present-day magmatic activity at LdM.

2. GNSS and InSAR data

Ground deformation at LdM was characterized from daily solutions at five continuous GNSS stations installed by the Observatorio Volcanológico de los Andes del Sur (OVDAS) covering a period of about five years (May 2012 to April 2017) (Fig. 2). SAR imagery over LdM was acquired by two satellite missions: C-band Interferometric Wide Swath mode images from the European Space Agency (ESA) Sentinel-1A/B (Table 1) and L-band Stripmap mode images from ALOS 1 and 2 operated by the Japan Aerospace Exploration Agency (JAXA). Full details on GNSS and InSAR processing can be found in Supplemental Section S1.

3. Time series analysis

The good agreement between the GNSS and InSAR data confirms the reliability of the InSAR processing (Fig. 3B). The subset of inverted InSAR time series (Fig. 3) indicates that C-band and L-band data exhibit a good coherence (>0.6) over most of the study area. The time series maps also reveal a displacement pattern affecting an elliptical area with a 26 km NNE-SSW major axis and a 19 km minor axis with a difference between ascending and descending tracks due to their difference in satellite viewing geometry. The resulting GNSS and InSAR time series are analyzed by applying a principal component decomposition using the decomposition algorithm available in PCAIM (Perfettini et al., 2010; Remy et al., 2014) (see details in Supplemental section S2.1). This analysis suggests that the shape of the displacement field remains nearly constant over the three-year period and that only the amplitude of the signal evolves linearly over time, indicating that the observed signal is mainly the result of a unique process.

3.1. Spatial and temporal patterns of the ground displacement at LdM

We benefit from the ascending and descending Sentinel-1 tracks to retrieve the easting and the vertical components of the ground displacement, allowing us to map the displacement field at LdM (see Text S2.2 for a detailed explanation). The resulting maps of vertical and horizontal displacement rates derived from Sentinel data from October 2014 to July 2017 are shown in Fig. 4A. Vertical displacement rates reach a maximum of 20 cm/yr, while maximum eastern displacement rates are lower reaching 10 cm/yr and 5 cm/yr for the displacement to the west and to the east, respectively. The easting displacement map exhibits clearly a double-lobe pattern along a N10°–N30° axis with a positive lobe pattern (displacement toward the east) much smaller than the negative one (displacement toward the west). Assuming a homogeneous crust, such a behavior suggests that the source roof is not horizontal. Another hypothesis is that this asymmetry is due to spatial variations in the mechanical properties of the rocks. However, in absence of more precise information on rock layering at depth, and given that a number of non-unique rock heterogeneities can explain similar displacement patterns (e.g. see review by Mastelark (2007), we choose to condense the information of this pattern into a single meaningful property, e.g. the roof of the magmatic source (there may be a gradational transition of the rock magma boundary, e.g. see discussion in Townsend et al., 2019).

We take advantage of the availability of the InSAR data acquired since 2007 by ALOS-1 satellite to extent the period of ground displacement measurements at the location of the GNSS station MAU2, which records is the highest rate of displacement at LdM. It was not possible to use ENVISAT data for this purpose since

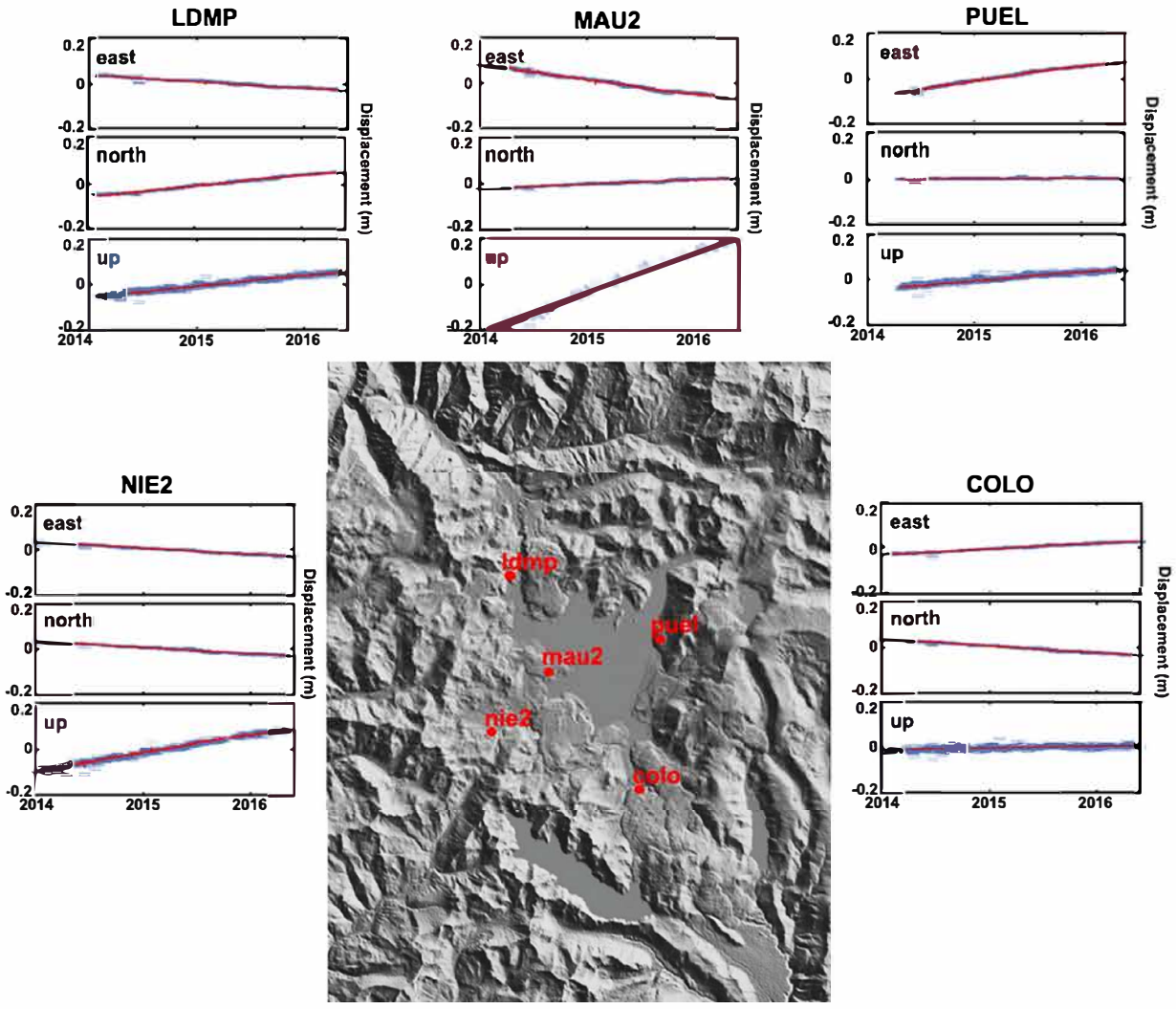

Fig. 2. Ground surface displacement at the five GNSS stations operating at LdM. The red circles and associated name show the location of the GNSS stations. Blue dots with error bars are the observed GNSS data with their 1σ uncertainty. Red line shows the reconstructed GNSS data using the first component of the decomposition.

Table 1
Summary of the processed SAR data.

Satellite	Mode	Orbit	Track	Mean incidence angle (°)	No. of SAR images	Start	End
Envisat	IM	Ascending	10	21	13	20030325	20061219
ALOS-1	IM	Ascending	112	38.2	8	20070126	20101222
ALOS-1	IM	Ascending	113	41.4	9	20070212	20110108
ALOS2	SM3	Descending	130	33	5	20150312	20170705
SENTINEL1	IW	Ascending	18	33.3	33	20141030	20170728
SENTINEL1	IW	Descending	83	33.3	32	20141023	20170721

only one interferogram formed from the C-band Envisat images acquired in March 2003 and February 2004 is coherent, and it does not reveal any displacements. Consequently, we generate two independent ALOS-1 InSAR time series from tracks 112 and 113, using a similar approach to the one used previously. As the LOS are very close for these two tracks, we can compare the two resulting InSAR time series. This comparison shows a good agreement between the two independent datasets providing confidence in our InSAR processing (Fig. 4B). In order to make the GPS vectors geometrically comparable with the InSAR data, we projected the GPS vector observed at MAU2 into the LOS of the track 112. To fill the gap between the end of InSAR measurement and the beginning of the acquisition at MAU2 we used the average velocity observed at MAU2 using ALOS1 data spanning the one-year period 2010–2011. In agreement with Le Mével et al. (2016), the reconstructed displacement time history recorded at MAU2 from January 2007 to July 2017 highlights a clear decrease of the displacement rate at MAU2 from 24.4 cm/yr for the period spanning January 2007 to January 2011 and 15 cm/yr for the period spanning October 2014 to January 2017 (Fig. 4B).

4. Mechanical modeling strategy

We first verify our assumption that the surface displacements measured by InSAR and GNSS could be related to a pressure increase in a massive source. To determine the most appropriate geometry of such a source, we consider a variety of classical analytical source geometries to model the surface displacements at

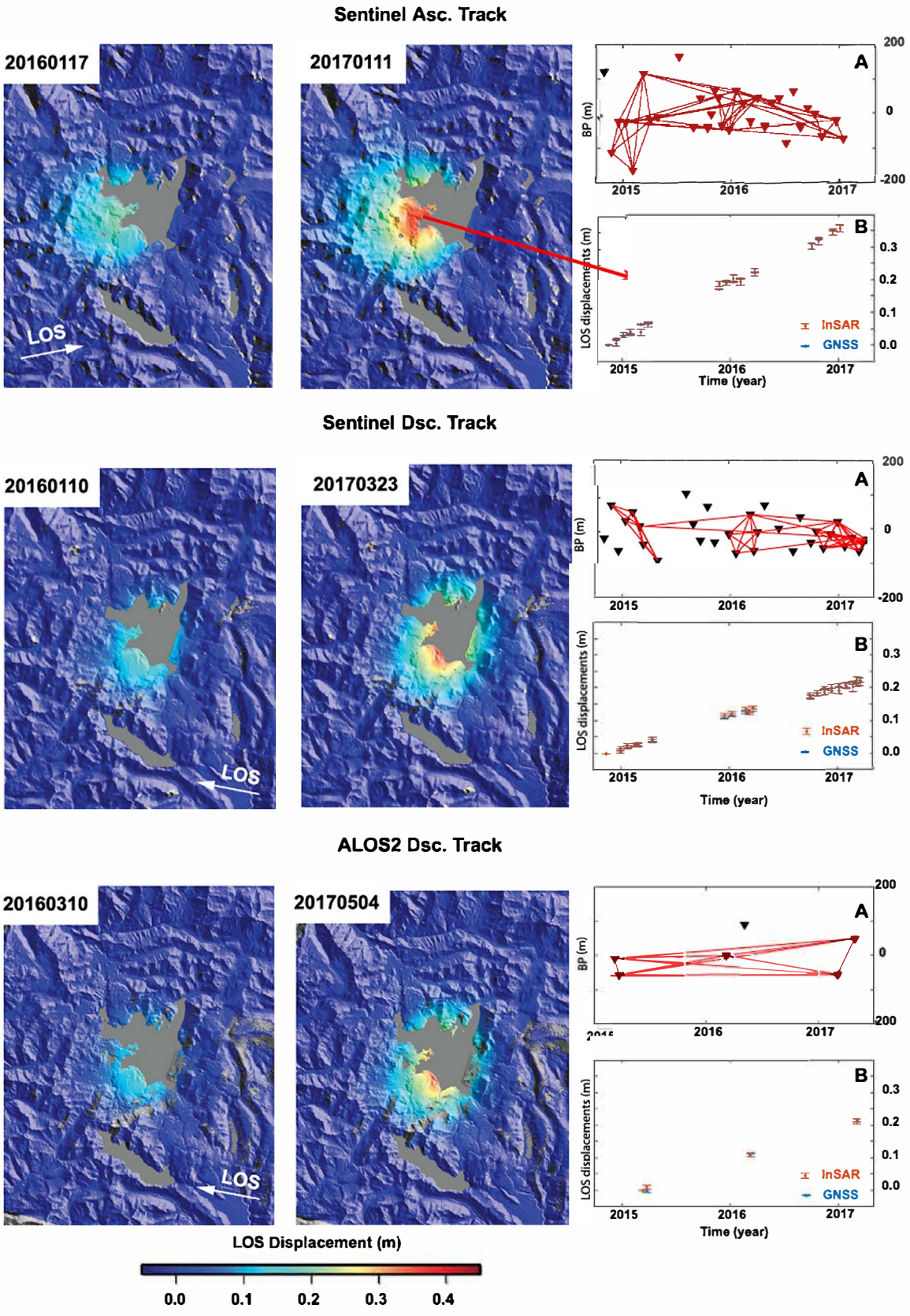

Fig. 3. Subset of adjusted LOS displacement maps overlaid onto a shaded relief map. Up) Ascending Sentinel track displacement maps from January 2016 and January 2017 with respect to the image acquired in October 2014. **A)** Perpendicular baseline (in meters) as function of time. Black triangles and red lines represent the SAR images and the interferograms used in this study. **B)** Cumulative LOS displacements and their 1σ uncertainties (in red) recorded at the location of the GNSS station MAUL2 and the GNSS vectors recorded at MAUL2 projected into the radar LOS (in blue). Middle) Same as previously but for the descending Sentinel track displacement maps from January 2016 and March 2017 with respect to the image acquired in October 2014. Bottom) Same as previously but for the descending ALOS2 track 130 displacement maps from March 2016 and May 2017 with respect to the image acquired in March 2015. The satellite to ground radar line of sight LOS is shown with a white arrow. LOS displacements toward the satellite are positive. The areas shown in gray indicate area which are not coherent.

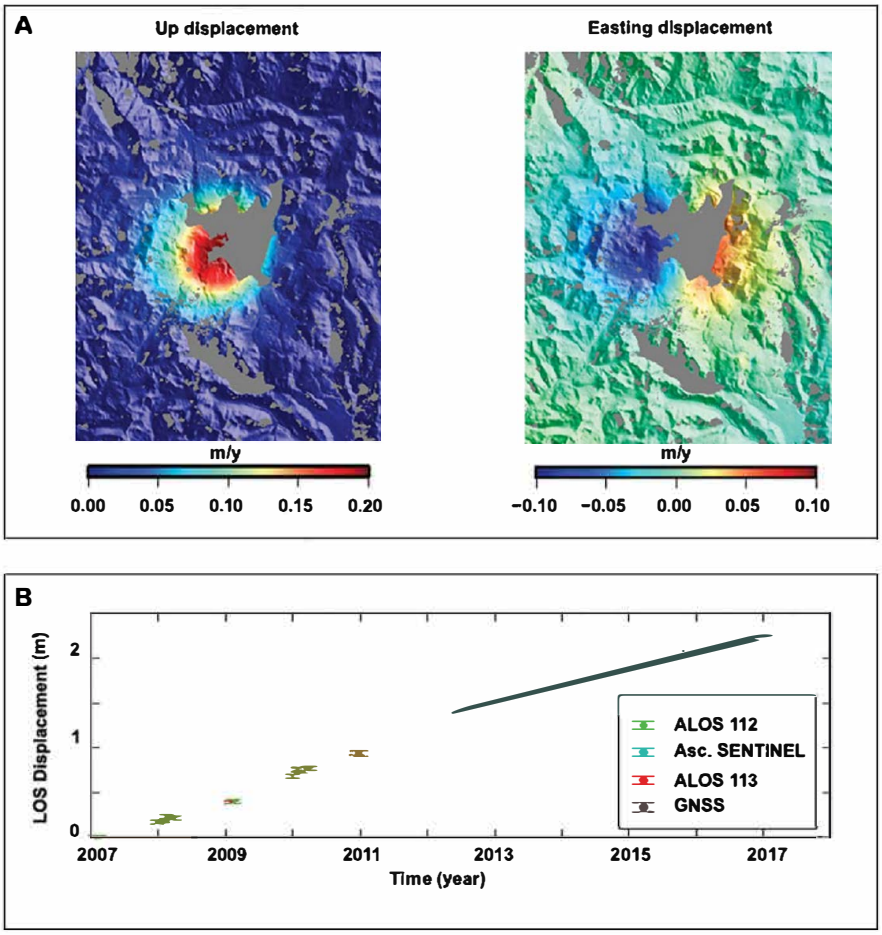

Fig. 4. Spatial and temporal behaviors of the ground surface displacement at LdM. A) Easting and vertical components of the mean displacement observed between November 2014 to February 2017 obtained from the combination of the ascending and the descending Sentinel InSAR data. Left) Vertical component of the ground surface displacement. Right) Easting component of the ground surface displacement where negative and positive values indicate displacement to the west and to the east, respectively. Different color scales are used between the two maps in order to improve the contrast between them. B) Time series of LOS displacements and their uncertainties for ascending ALOS1 InSAR and Ascending Sentinel data at the location of the GNSS station MAU2.

LdM (more details are in Supplemental section S3). Inversions favor flat-topped sources rather than spheres or prolate ellipsoids (see Supplemental Table S1), in agreement with the estimated ratio of maximum horizontal to maximum vertical displacement, equal to about 0.31 according to GNSS measurements (Dieterich and Decker, 1975; Remy et al., 2014). Therefore, we explore how a large and wide flat-topped pressurized cavity immersed in an elastic crust, can simulate a reservoir filled with a low-viscosity magmatic fluid. We assume that the pressure increases within this large and wide flat-topped reservoir, with the shape of an elliptical truncated cone. In a second step, and following authors like Jellinek and DePaolo (2003) or Le Mével et al. (2016) who considered a viscoelastic upper crust, we search for a model that would simulate the intrusion of new magma at the base of a large silicic mush reservoir itself acting as a viscoelastic boundary zone. We assume that this large reservoir is composed of largely crystallized rhyolite close to the solidus temperature (670 °C) or of country rock heated above the brittle-ductile transition (500–600 °C), as was deduced from geochemical and thermodynamic models for LdM (Andersen et al., 2017; Miller et al., 2017). We also assume that the timescale of surface deformation is very small compared to the temperature evolution of the system, with a diffusive timescale $\tau = L^2/k \sim 1$ Myr ($L \sim 5$ km the characteristic width of the reservoir and $k \sim 10^{-6}$ m^2/s the thermal diffusivity). Therefore, it is reasonable to consider a steady-state temperature, and consequently we define a steady-state viscosity inside a shell that behaves according to Maxwell viscoelasticity (Del Negro et al., 2008; Currenti and Williams, 2014; Segall, 2016 and references therein). The main difficulty then stands in inferring the geometry of this reservoir. First, we verify that our finite-element method Adeli-3D (Hassani et al., 1997), which accounts for viscoelasticity, matches classical analytical solutions (e.g. Segall, 2010, details presented in Supplemental section S4). Then, we compare the results produced by Adeli-3D with those produced by the 3D-boundary-elements method MC3 (Cayol and Cornet, 1998) that accounts for elasticity only. Therefore, we compare the surface displacements produced by a truncated cone embedded in an elastic domain (with MC3) with those produced by this same truncated cone acting as a viscoelastic shell at the base of which a small pressure source is defined (with Adeli-3D). Our results show that both models produce the same patterns of ground surface displacements after enough time allows for the complete transfer of pressure from the inner source to the visco-elastic shell walls. This convergence, is expected from analytical models (Segall, 2010, for further details refer to Supplemental section S5). Therefore, taking these results into account, we first invert the observed ground surface displacements considering that they are triggered by a pressure increase in an elliptical truncated cone embedded in an elastic medium (section 4.1), and second we use the geometrical parameters inferred from that inversion to explore the influence of a viscoelastic response of this truncated cone on the temporal evolution of displacement field (section 4.2).

Table 2
Parameters of the different ground deformation models. X and Y are the location of the source center expressed in km (UTM WGS84 zone 19 South). Depth is the depth below the mean surface elevation (i.e., 2500 m asl). V is the volume of the elliptical truncated cone. ΔV is the rate of volume change from October, 2014 to July 2017. ΔP is the rate of pressure change from October, 2014 to July 2017. S_1 is the major axis and S_2 the minor axis. Strike is clockwise angle relative to the north, Dip is the dip angle of the minor axis, alpha is the dip angle of the source wall with the following convention, alpha <0 the source walls dip outward (*i.e.* a cone which widens downward) and alpha >0 the source walls dip inward (*i.e.* a cone which narrows downward). ΔP and ΔV are the rate of pressure and of volume changes from October, 2014 to July 2017, respectively. V is the volume of the elliptical truncated cone estimated from the geometrical parameters inferred from the inversion. χ_r^2 is the value of the fit of model to data. t_1 is the loading time, η: the viscosity, P the pressure in the basal magmatic intrusion and rms is the root mean square difference between modeled and observed displacement at MAU2.

Model form	Model 1	Model 2	Model 3
	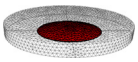	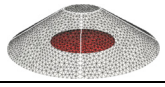	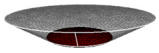
Parameters inferred from elastic inverse models			
X position (km)	361.267	361.948	360.949
Y position (km)	6007.115	6006.876	6007.321
Depth (km)	5.42	3.00	5.15
S_1 (km)	11.52	3.00	12.58
S_2 (km)	8.92	2.22	8.85
Strike (°)	23	25	24
Dip (°)	−19	−23	−23
Height (m)	1000	3000	2000
Alpha (°)	0	−60	59
ΔP (MPa y^{-1})	1.35	1.45	1.66
ΔV (km^3 y^{-1})	0.0214	0.0190	0.0205
V (km^3)	80.97	137.17	100.75
χ_r^2	1.07	1.08	1.08
Parameters inferred from visco-elastic inverse models			
t_1 (days)	1980.95	1742.5	1549.36
η (Pa s)	9.97e16	9.5e16	9.94e16
P (MPa)	36	18.7	23
rms (m)	0.04	0.02	0.01

4.1. Modeling of ground deformation with an elastic rheology

To determine the best fitting reservoir geometry, we use MC3 for linear elastic media (Cayol and Cornet, 1998) and the following inversion scheme. For all model cases, we assume a homogeneous crust with Poisson's ratio of 0.25 and a shear modulus of 13 GPa obtained from the velocity model from Cardona et al. (2018), assuming a constant density of the upper crust of 2500 kg/m^3. In agreement with the result of the decomposition, we invert only the first principal component of the different data set in order to search for the geometries that best explain the data, rather than inverting the displacement data available at each epoch. Next, we use the resulting best geometries for the elliptical truncated cone to compute the pressure history of the sources using the same approach as Remy et al. (2014). The inversion is performed using a neighborhood search algorithm (Sambridge, 1999a, 1999b), which finds optimal values of the parameters by minimizing the chi-square and allows for a detailed exploration of the parameter space. The reduced chi-square (χ_r^2) of the residuals between observations and modeled displacements used to compare the goodness of fit of the data to the models is given by:

$$\chi_r^2 = \frac{1}{N-k}\sum\left[\frac{X_{obs}-X_{mod}}{\sigma}\right]^2$$

Where N is the length of data and model vectors, k is the number of free parameters of the model, X_{obs} and X_{mod} are the observed and the modeled displacement and σ is the data uncertainties. The elliptical truncated cone source depends on the ten parameters listed in Table 2. As already observed in Remy et al. (2014), the inversion indicates that the geographical location, the azimuth of the displacement source and the dip of its major axes are well resolved. However a trade-off appears when constraining the depth, thickness and dip of the source walls, leading to a continuum of acceptable models with a depth ranging from 2000 m to 6000 m. This trade-off leads also to a strong uncertainty on the determination of the source volume which varies from about 50 km^3 to 200 km^3. Nevertheless, whatever the source considered, the value of the rate of volume change is very similar and close to 0.02 km^3/yr from October 2014 to January 2017. Table 2 presents three characteristic models from the continuum of acceptable models that are able to match the data. These models provide slightly lower values of χ_r^2 than the Okada-type dislocation model (see Supplemental Section S3). Nevertheless, similarly to the Okada-type dislocation model (χ_r^2 of 8.50), they fail to properly match the GNSS data (χ_r^2 of 6.50) essentially due to significant discrepancies between the observed and the modeled horizontal displacements, in particular at station PUEL. On the other hand, χ_r^2 for the InSAR data increases with the time span between a given InSAR time series map and the reference image used for the least square adjustment, due to the presence of localized residual patterns located around the lake. Possible explanations for this misfit pattern can be that the geometry of the source is more complex than the simple truncated cone used here, or that subsurface heterogeneities alter the ground displacement. In Fig. 5 we compare the displacement observed on the largest period of each track and on a three-year 2014–2017 period of GNSS data with the modeled displacements using one of the best elliptical truncated cones (Model 3 in Table 2). In order to check if these models are able to reproduce the ground displacement field observed since 2007, we use them to invert the best interferograms obtained from ALOS1 (Supplemental Figs. S19 and S20). Considering that these models still adjust well the data, yielding χ_r^2 of about 1, we conclude that it is reasonable to assume that the source of ground surface displacements has not changed significantly neither in shape nor in location since 2007.

4.2. Modeling of ground deformation with a visco-elastic rheology

In this section, we model the temporal evolution of the ground displacement caused by a source simulating an intrusion of mafic magma located at the base of a viscoelastic mush reservoir immersed in an elastic crust. First, we use the 3D finite-element code ADELI (Hassani et al., 1997), which has been used to simulate a variety of geodynamical contexts, including long-term deformation at subduction zones (Hassani et al., 1997; Cerpa et al., 2015) and short-term interseismic deformation (Contreras et al., 2016). This code uses a time-explicit dynamic relaxation method (Cundall, 1988) to solve the quasi-static equation of motion, and can handle a variety of visco-elasto-plastic rheologies. More details can be found in Chéry et al. (2001), Cerpa et al. (2015) and Gerbault et al. (2018). The modeled mesh domain includes an elliptical truncated cone embedded in a surrounding elastic crust, with a pressurized ellipsoidal source at its base simulating magma recharge. Maxwell visco-elasticity is assumed inside this elliptical truncated cone, to simulate a crystal rich mush reservoir in agreement with Dragoni and Magnanensi (1989), who showed that this rheology reproduces well the behavior of volcanic rocks at high temperature. Supplemental section S4 provides benchmarks of ADELI with solutions for a viscoelastic shell in an infinite medium (Dragoni and Magnanensi, 1989) and with solutions accounting for a free surface (Segall, 2010), illustrating that a resolution of 100 m is required to generate accurate solutions. We test a full 3D model geometry: the modeled domain is a cube of lateral extent 80 km, large enough to minimize border effects. The mesh is composed of a total of $6{,}9 \times 10^5$ elements, with highest resolution (100 m) between the source and the free surface above (Fig. 6A). The LdM is not a high-

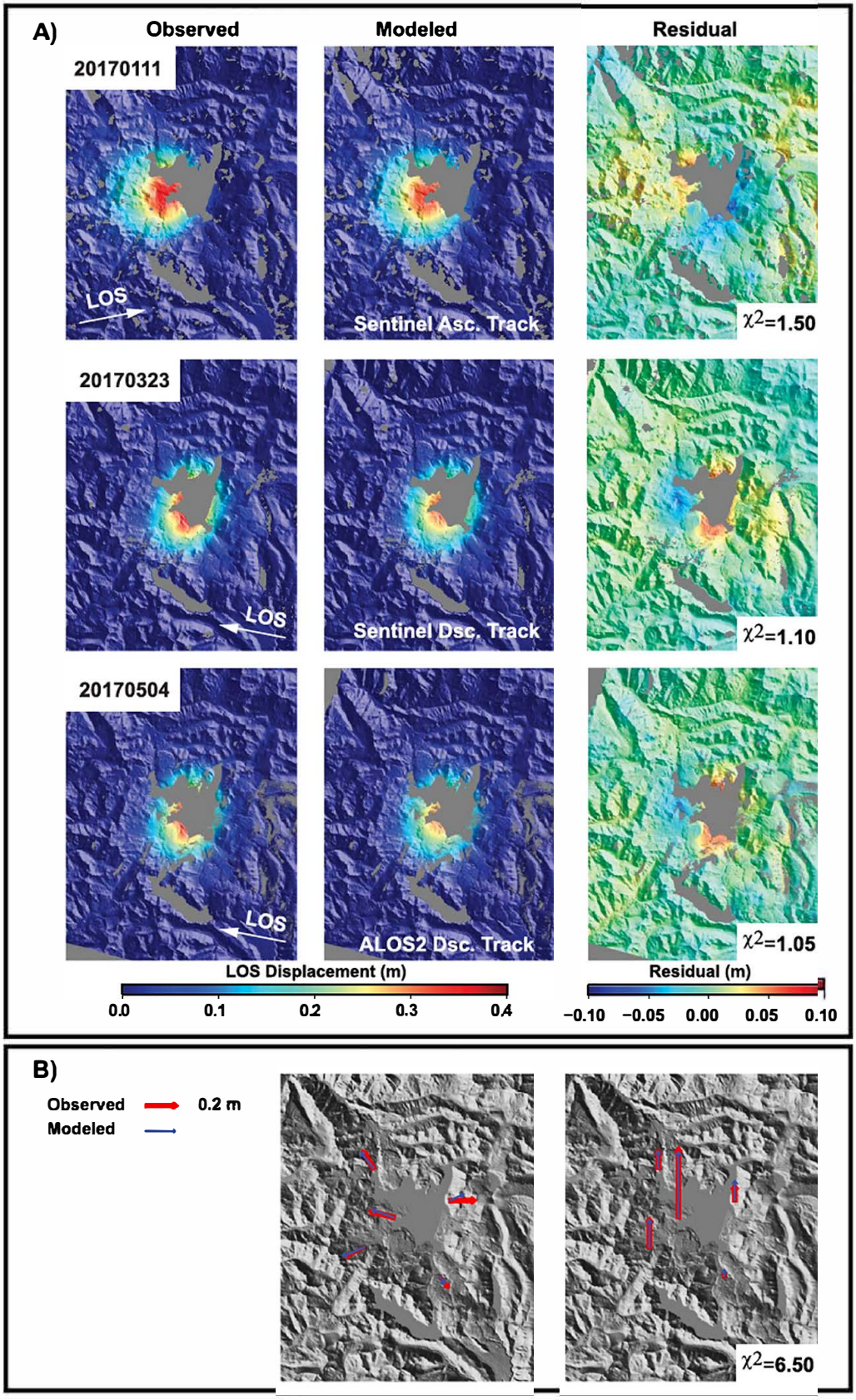

Fig. 5. Maps of the observed and modeled GNSS and InSAR data using one of the best elliptical truncated cone model. A) Upper, middle and bottom Example of three LOS displacement maps, the model prediction and the residuals between observed and modeled data. B) Observed cumulated Horizontal and vertical GPS displacements (red vectors) from 2014 to 2017 and modeled displacements (blue vectors).

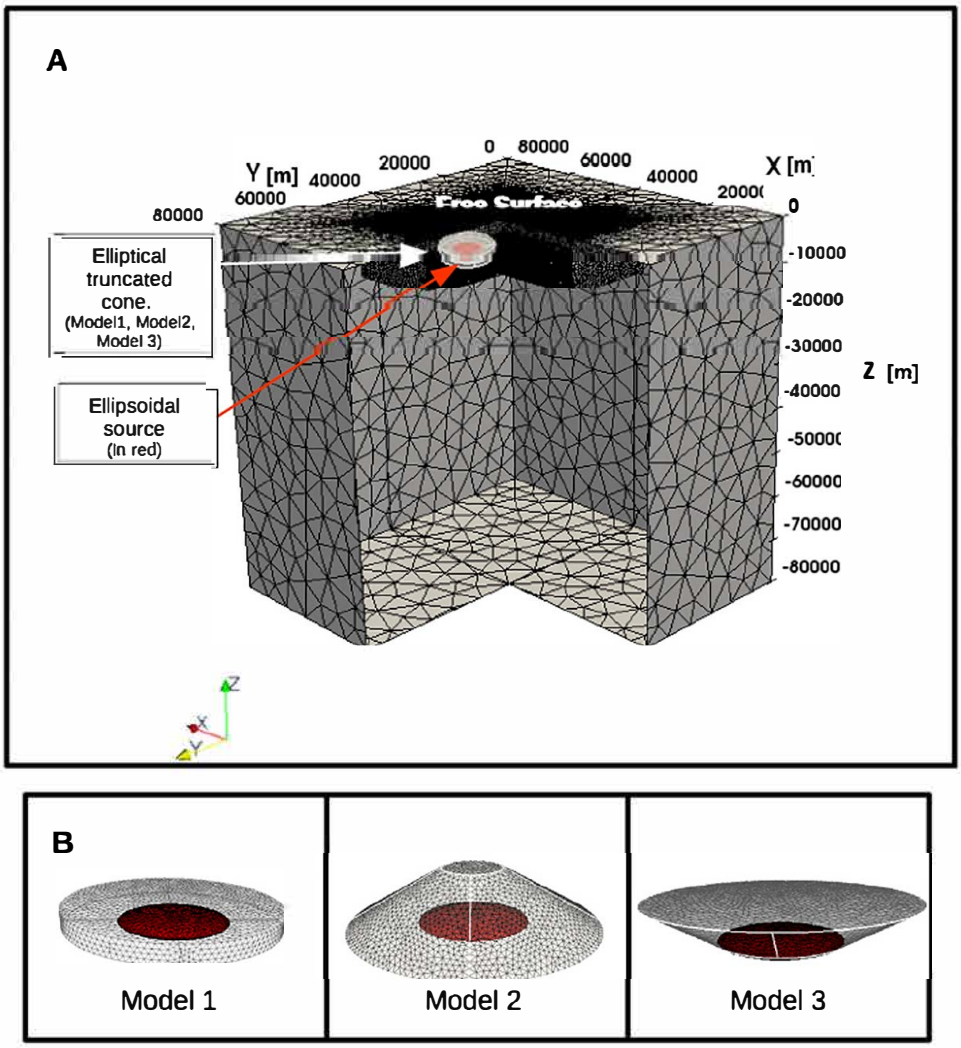

Fig. 6. Mesh geometries for the finite element ADELI setup. A) The model is meshed with tetrahedral elements with high resolution in the source and up to the free surface close to the source. B) Meshes used in the viscoelastic models. The ellipsoidal source (in red) and the viscoelastic elliptical truncated cone (in grey) are meshed with a resolution of 100 m.

relief volcanic edifice and the topographic slope in the area is less than the limit of 10° for which its effects become significant (Cayol and Cornet, 1998), therefore we define a planar top-free surface. We use the three characteristic chamber's geometries found in the previous section (Table 2), since the cumulated surface displacement does not change between an elastic model and a viscoelastic model (Supplemental section S5) (Dragoni and Magnanensi, 1989; Bonafede and Ferrari, 2009). Without reliable information concerning the geometry of the basal magmatic intrusion, we choose to apply a pressure increase within a small ellipsoidal source (volume of 10 km^3) situated at the base of the large elliptical truncated cones (Fig. 6B).

A trapezoidal function over time is then used to model the variation of pressure inside a thin ellipsoidal source located at the base of the large viscoelastic shell (as in Newman et al., 2001; Segall, 2010; Del Negro et al., 2008; Parks et al., 2015). During the first period, pressure increases linearly between 0 and t1 simulating a recharge of new magma mass at constant rate into an existing reservoir. During the second period, pressure remains constant, which means that the characteristic time scale of the major processes of i) injection supply rate and ii) internal precipitation and exsolution rates are basically slower than the relaxation time of the viscoelastic shell, at the scale of the 10 yr period of measured surface deformation and over the breath of the volcanic complex. During this second period, the pressure within the viscoelastic shell progressively evolves with time, from its base to its outer extremities (walls). Maximum ground surface displacement is achieved when this pressure is totally transferred to the walls and the roof of the visco-elastic reservoir. Consequently at this moment, the surface displacement pattern coincides with that obtained assuming a purely elastic medium, with a discrepancy less than 5% (Pascal et al., 2013, Supplemental section S5). This behavior illustrates that the surface displacements pattern is clearly dominated by the pressure increase at the walls of the visco-elastic domain rather than by the pressure inside the smaller ellipsoidal reservoir, as shown by previous authors with spherical sources (Dragoni and Magnanensi, 1989; Bonafede and Ferrari, 2009).

In order to reproduce the temporal evolution of LOS displacements at MAU2, we solve the inverse problem and fit these displacements with our visco-elastic model according to the following approach. A grid method is used to sample the $\log_{10}$ of the viscosity (η) on the truncated cone mush reservoir, bounded by lower and upper limits of 15 and 18, respectively (See Supplemental Fig. S21). The choice of these limits is based on different theoretical studies (Dragoni and Magnanensi, 1989; Bonafede and Ferrari, 2009), thermomechanical models (Jellinek and DePaolo, 2003; Del Negro et al., 2008), and laboratory experiments of silicic volcanoes

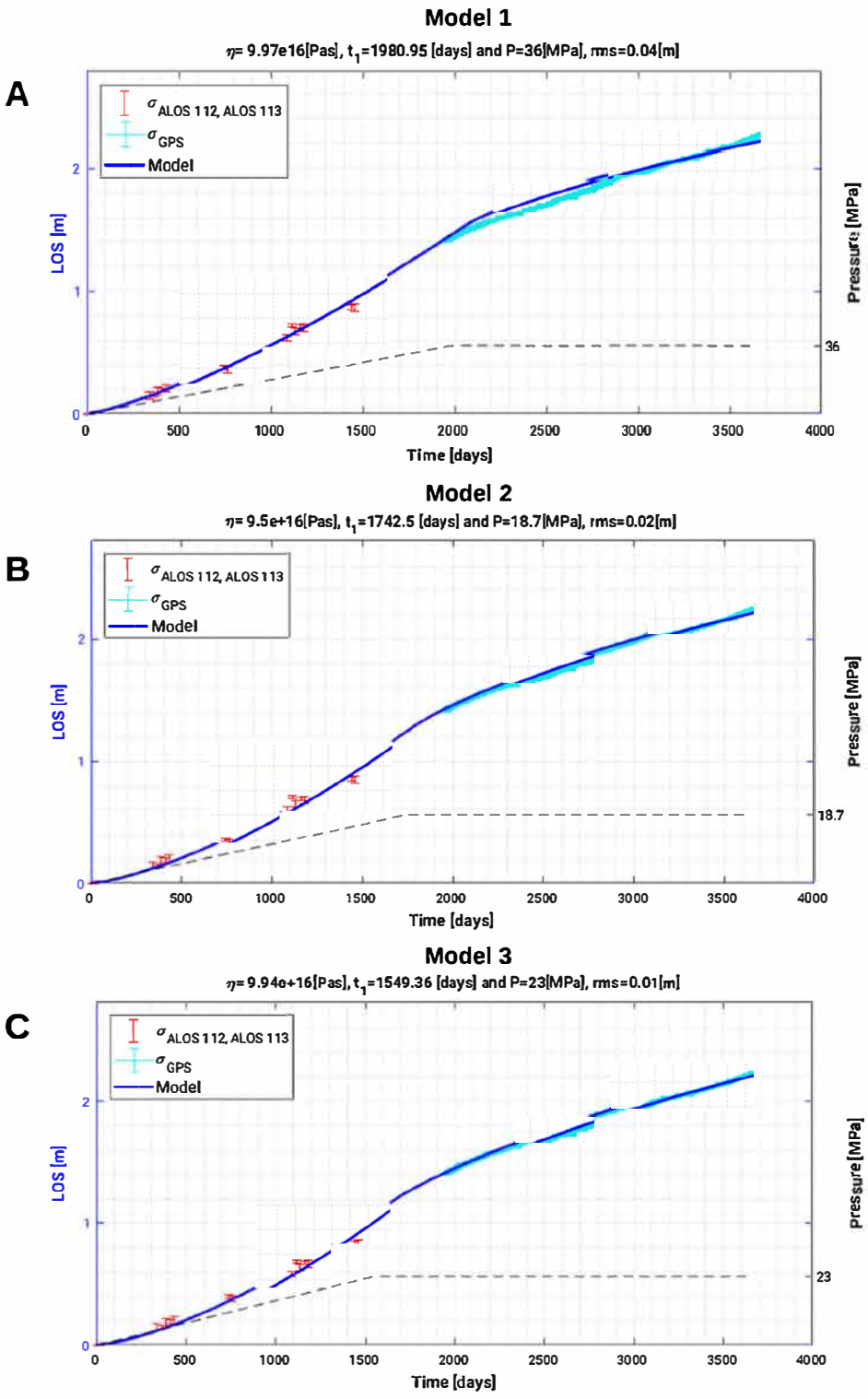

Fig. 7. Results of the best fit of the temporal evolution of surface displacements at MAU2 in the last 10 yr (3650 days). The upper, middle and bottom figures represent the three different elliptical truncated cone models used in this study, which simulate an elliptical truncated cone that responds viscoelastically to the inflation of an ellipsoidal source at its base. The upper panel of each figure includes the parameters associated to the best model η: viscosity, t_1: loading time, P: pressure, and rms: root mean square error.

(Newman et al., 2001, 2006). Then, a Levenberg-Marquardt numerical optimization grid search method determines the optimum loading duration of the magma injection (t_0) together with the optimum overpressure (dP) inside the ellipsoidal source and the optimum viscosity (η) in the visco-elastic cone truncated (Levenberg, 1944). We limit the range of duration of this magma injection from several months to 10 yr and the overpressure from 1 to 150 MPa. We present on Fig. 7, the different viscoelastic models inferred from each geometry, that best match the observed 10 years-long time series of ground displacements at MAU2 (spanning period 2007–2017).

The resulting viscosities (η) in the truncated cone reservoir are very similar in all three model geometries. Nevertheless, the duration of the loading time (t_0) and the pressure (dP) differ slightly.

The best minimum root mean square (rms) error between observed and modeled ground surface displacements are obtained for a viscosity $\eta \sim 10^{17}$ Pa s in model 1, model 2 and model 3; resulting in rms values of 0.04, 0.02 and 0.01 m, respectively. The loading time varies between $t_0 \sim 4$ yr for model 2 and model 3, to a maximum $t_0 \sim 5.4$ yr, for model 1 supporting the idea that the mafic recharge could not have been longer than the first 6 yr and that the remaining deformation was caused by the viscoelastic response of the surrounding shell. The applied overpressure in the elliptical source at the base of the truncated cones varies slightly showing that a thicker viscoelastic reservoir requires less overpressure to generate similar ground surface deformation; dP ranges from 18 MPa for the thickest viscoelastic source (3 km height) to 36 MPa for the thinnest source (1 km height). The appropriateness of these values are further discussed in the following section 5.

5. Discussion

5.1. Source characterization

This study confirms that the uplift at LdM started sometime between 2004 and 2007 (Fournier et al., 2010; Feigl et al., 2013) and continued at least until March 2017. The decomposition of both InSAR and GNSS time series indicates that displacements have been linear in time since early 2012. The best inflating truncated cone models embedded in an elastic crust, deduced from the inversions of Sentinel 1 and GNSS data match well the ALOS1 data acquired from 2007 to 2011, indicating that the source's shape and location have not changed significantly since 2007. Our inversions show that the center location, the orientation and the dip of the source remain very similar whatever its geometry. The center is located below the southwest part of the lake, its major axis is elongated N22°E–23°E and it dips down to the west with an angle of about 20°. Furthermore, the inversions cannot provide strong constraints on the depth of the source, due to the trade-off between depth and pressure. Nevertheless, the estimated rate of volume change, of about 0.02 km^3/yr from October 2014 to January 2017, is close to that obtained by Le Mével et al. (2016) and is independent of the source type when assuming a purely elastic crust and an incompressible magma.

5.2. Visco-elastic parameters of the mush reservoir

A large spectrum of acceptable source geometries explains the data, ranging from a thin source (sill) to a large massive source of equivalent basal area of about 10×8 km^2. The volume and the thickness of this large massive source range from ~60 to 200 km^3 and from 1000 to 3000 m, respectively. Such values might seem large, but they are compatible with the size of the magma chamber that would have triggered the formation of the 12×8 km^2-wide Bobadilla caldera ~950 kyr ago (Hildreth et al., 2010). From the continuum of possible sources, we selected three representative geometries simulating a mush reservoir that responds visco-elastically to a basal pressure change. Whatever the geometry considered, they fit the temporal evolution of surface displacements at MAU2 for a viscosity converging towards 10^{17} Pa s. Our results indicate that a thicker mush reservoir (model 2 and 3 in Fig. 7B–C) explains better the temporal evolution of surface displacements than the thinner model 1 (Fig. 7A). Model 1 cannot explain the variation in slope that starts in 2014 (day ~1980, Fig. 7A), illustrating the importance of the thickness of the mush reservoir in amplifying surface displacements.

The presence of a large mush reservoir beneath LdM has two main implications. (i) Although an elastic medium requires a full 10 yr of inflation over the 10 yr of observed surface uplift, a visco-elastic medium "overtopping" an ellipsoidal source requires a shorter period of active inflation (less than 6 years), the remaining four-years reflecting its delayed visco-elastic response. (ii) Although the cumulated surface displacements are similar between an elastic medium and a visco-elastic medium, the visco-elastic mush model requires less basal magma recharge, *i.e.* a volume change 50% lower than the elastic model.

According to Le Mevel's model, a 25 km deep reservoir would feed a 30–60 m wide conduit with mafic magma during the first 2 yr (2007–2009) at a constant increasing pressure rate, itself filling in a shallow crustal reservoir. Over the following years, the pressure remains constant in the deep reservoir, but it continues to increase in the shallow reservoir until hydrostatic equilibrium is reached. This model explains both the amplitude and the progressive deceleration of the ground surface displacements with the elastic response of the bedrock surrounding the upper chamber. Le Mével et al. (2016) justify their assumption of an elastical bedrock by showing that a viscous component of deformation increments the surface uplift by only 4% compared to a purely elastic solution. But these authors assumed that the viscoelastic shell corresponds to the thermal variation associated to a mafic intrusion into a small magmatic source (16 km^3), thus insufficient to significantly amplify ground surface displacements. This would imply a continuous supply of magmatic material from below. Our assumptions here differ from Le Mével et al. (2016) because we consider a thicker mush reservoir developing over at least 26 kyr, hypothesizing that it would be continuously reheated with mafic magma during that broader time-scale. This assumption is coherent with the process suggested by Andersen et al. (2017) and others pointing towards the presence of a long-standing near-solidus magma body beneath the area of active uplift, cf. Section 5.3 below.

5.3. Large near-solidus magma body beneath LdM

The volume of the "mush" reservoir inferred by the inversion of InSAR and GNSS data must be taken with caution as we did not account for the possible contribution of additional viscous and brittle deformation of the bedrock around and below the reservoir. This host rock could be mechanically damaged by dyking and metamorphic reactions in a potentially hydrated environment, which would contribute to further reducing its effective strength (Rubin Allan, 1995; Newman et al., 2001; Jellinek and DePaolo, 2003; Gerbault et al., 2018). The viscosity of about 10^{17} Pa s inferred from our modeling study is one order of magnitude below common values of crustal viscosity ~10^{18} Pa s inferred for volcanic regions with a large amount of heated country rock (Newman et al., 2006; Parks et al., 2015; Le Mével et al., 2016), but it is higher than that obtained in other thermo-mechanical studies such as those of Del Negro et al. (2008) and Currenti and Williams (2014) that obtained a crystal viscosity of ~10^{16} Pa s. This value of 10^{17} Pa s is in turn too high to support the hypothesis of a large quantity of molten magma beneath the LdM volcanic complex, which is in agreement with the main conclusions of the MT analysis carried out by Cordell et al. (2018), who suggested that a molten magma body below the uplift area was unlikely to be greater than 10–20 km^3. Our modeled values are also consistent with the gravity anomaly pattern reaching 19 mGal at the center of inflation, which was interpreted to witness a large shallow silicic system of low density, mostly crystallized magma (Miller et al., 2017). It is also consistent with the results of isotopic geochemical studies that rule out the possibility of LdM rhyolites being generated in the lower crust, and rather favor the hypothesis that the last period of activity resulted from mafic magma intruding a well-developed pre-existing crystallized rhyolitic reservoir in the shallow crust (Andersen et al., 2017).

Jellinek and DePaolo (2003) pointed out that the accumulation of large quantities of magma for many years in silicic vol-

canoes is favored by warm-wall rocks with lower effective viscosity compared to conventional bedrocks. Conjointly for silicic volcanoes, Cooper and Kent (2014) suggested for Mount Hood, USA, that nearly all of the duration of magma storage (>88% and perhaps 99%) occurs at near-solidus conditions, *i.e.* under relatively cool (<750°), viscous and uneruptible conditions. They suggested that eruptions in these systems occur via remobilization of a cold and rigid state that reacts immediately to mafic recharge, as had also been suggested for other silicic volcanoes such as Taupo volcano, Long Valley, and others (Charlier et al., 2004; Hildreth, 2004; Hildreth and Wilson, 2007; Cooper and Kent, 2014; Degruyter and Huber, 2014). This concept of magma storage is also similar to that proposed in the recent study by Szymanowski et al. (2017) from the analysis of zircon and titanite crystals collected in the Kneeling Nun Tuff (New Mexico). These authors conclude that magma has been mainly stored at cold temperatures ranging from 680 to 730°. Therefore, despite the detection by MT of a large partially molten magma body in the northern zone of LdM, which could forecast an imminent eruption, the small volume of high melt concentrations immediately below LdM probably reflects that the mafic recharge is not able to promote an eruption. A large near-solidus magma body beneath LdM maintained in a non-eruptible state, might still be reactivated before an eruption, but not necessarily "enough".

A significant influx of magma over a long period of time is still required to allow for the development of a long-lived large near-solidus magma body (Annen, 2009; Galetto et al., 2017), or else diffusive cooling would freeze it. At LdM, the abundance and the frequency of post-glacial rhyolitic eruptions are characterized by a prolonged history of explosive silicic eruptions since 1.5 Ma (for instance the Bobadilla caldera collapse ~950 ka ago, Hildreth et al., 2010). The development of this high crystal rich reservoir with successive transient mafic recharges might be linked with the >60 m magnitude of surface deformation accumulated since 9.4 thousand years in the southern-east zone of LdM, and that was interpreted as the evidence for the incremental growth of a magma reservoir just underneath (Singer et al., 2014, 2018). Another hypothesis is that the LdM complex is fed from a large magmatic system at >8 km of depth to the north that could provide sufficient heat and melt to maintain the shallower system (Reyes-Wagner et al., 2017; Cordell et al., 2018). Finally, several studies converge to the same interpretation that the past 50 rhyolitic eruptions that encircled the lake in the postglacial period were derived from a single and large shallow silicic system of low density. This silicic magmatic system together with volatile mingling within it would furthermore inhibit the direct ascent of mafic magma to the surface (Hildreth et al., 2010; Singer et al., 2014; Miller et al., 2017; Andersen et al., 2017).

5.4. Implication on the source overpressure

The three representative geometries of viscoelastic truncated cones that we tested match the observed evolution of ground surface displacements with a maximum residual of 4 cm between models and observations. The models require a basal overpressure source ranging between 18 MPa for the largest viscoelastic reservoir (3 km thick, model 2) and 36 MPa for the thinnest viscoelastic reservoir (1 km thick, model 1). This pressure/thickness relationship can be justified with a simplified 1D analogy: considering a similar total surface uplift or deformation rate (dv) and a similar viscosity (η) for both geometrical domains, but a different height H_1, H_2 over which this deformation occurs, one can write $dv = H_1 \times P_1/\eta = H_2 \times P_2/\eta$ (invoking the standard stress-strain-rate viscous constitutive relationship). This leads $P_1 \times H_1 = P_2 \times H_2$, showing that the thicker the viscoelastic domain, the smaller the overpressure required to produce the same uplift rate. Such overpressures remain realistic since 18 MPa is of the order of the tensile strength of crustal rocks and a common value assumed for overpressurised magmatic crustal reservoirs. 36 MPa is also likely possible in contexts of rather dry and competent bedrock environments (Jellinek and DePaolo, 2003; Gerbault et al., 2018).

Finally, our study confirms that viscoelasticity is a key factor to promote long-term surface displacements over decades. Our model 3 in particular, which best fits the data between 2007 and 2017 at LdM, predicts that a four-year continuous injection of mafic magma at the base of a mush reservoir can promote 3.8 m of cumulative displacements at station MAU2 within 50 yr (Fig. 8). This increase reflects the slow transference of overpressure between a pressurized basal source and the walls of the large mush reservoir, due to its retarded viscoelastic response. While an elastic model is a good indicator of the pressure at the walls of a large source (if related to a small injection of magma over a short period of time) it cannot reflect the activation of a large magma chamber for silicic volcanoes displaying long-term deformation such as LdM. In such cases viscoelastic shells should rather be considered. Future measurements will help clarify the geometry of this large visco-elastic shell, and the associated inflating overpressure, further helping to predict the evolution of this volcanic hazard.

6. Conclusion

Our study quantifies for the first time the characteristic properties of a mush reservoir promoting large surface displacements above a silicic volcanic system such as LdM, Long Valley, Campi Flegrei, etc. Such large mush reservoirs may be associated to recurrent mafic recharges that these volcanic complexes experience, but do not necessarily indicate imminent eruption.

From the analysis of a 10 years-long combined time series of InSAR and GNSS data we first confirm the spatial and temporal evolution of the regional uplift (up to 2 m of accumulated displacement) observed at the LdM volcanic complex. As an alternative to previously proposed models explaining such surface displacements, we tested 3D visco-elastic models simulating a mafic magma recharge at the base of a crystal rich reservoir behaving visco-elastically. The tested geometries of visco-elastic reservoirs match the observed evolution of ground surface displacements over time, with a viscosity approaching 10^{17} Pa s. The resulting overpressure ranges between 18 and 36 MPa depending on the reservoir's dimension. Our models support a scenario in which a basal mafic intrusion first inflated during the first 4 or 6 yr of active deformation, then triggering a continuous slow transfer of pressure between this basal load to the viscoelastic reservoir's walls, promoting an increase in ground surface displacements for up to another 50 yr.

Our best fitting dimensions, viscosity and overpressure of the visco-elastic mush reservoir are consistent with previous interpretations of a large long-lived, near-solidus magma body underneath LdM. This raises the issue of how such magma bodies are thermo-mechanically maintained over time, by other mechanisms than standard thermal diffusion/dyking processes (metamorphism, percolation through porous media etc.), and calls for improving our understanding of the multi-scale physics of volcanic plumbing systems, also with the help of high quality geophysical and geodetic campaigns.

Acknowledgements

ASAR data were provided by the European Space Agency (ESA) through the project ENVISAT-AO#857 and Category 1 #2899. PALSAR data from the ALOS satellite mission operated by the Japanese

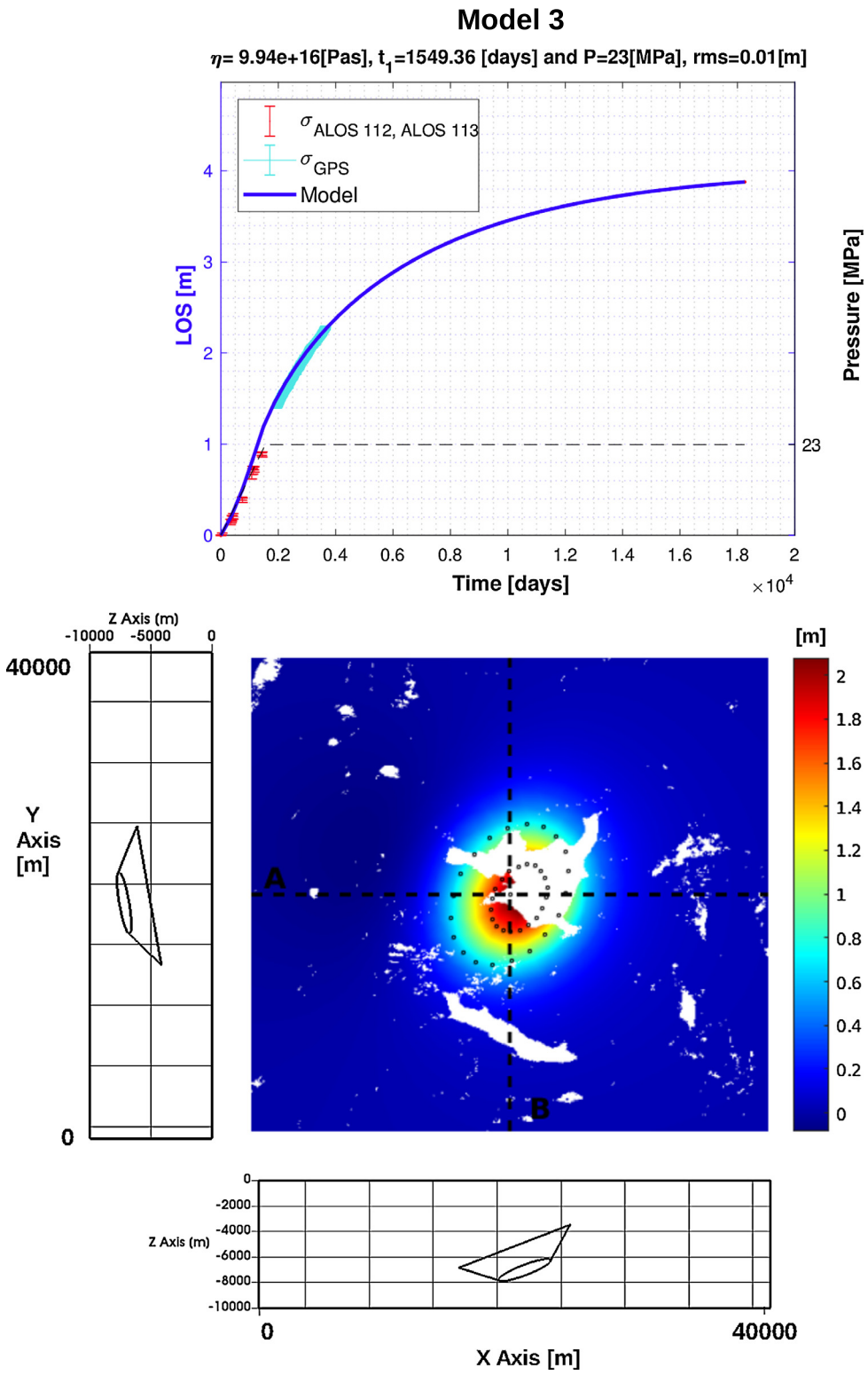

Fig. 8. Predicted spatial and temporal evolution of the ground surface displacement from model 3. **Up**) Modeled temporal evolution of the surface displacement at MAU2 for the next 50 years. **Bottom**) Modeled accumulated ground surface displacements from 2007 to 2017.

Aerospace Exploration Agency (JAXA) were used under the terms and conditions of the fourth ALOS 2 Research Announcement (project 1142). We thank the European Space Agency for providing us SENTINEL and ENVISAT data and OVDAS- SERNAGEOMIN for providing the GNSS data. C. Novoa acknowledges CONICYT-Becas Chile for her PhD scholarship (folio: 72170643). A. Tassara acknowledges support from FONDECYT (project 1151175). F. Delgado acknowledges Centre National d'Etudes Spatiales for a postdoctoral fellowship. We thank R. Hassani for his useful help with the Adeli software. The editor Tamsin Mather and the two anonymous reviewers provided useful and constructive suggestions that greatly improved this study. Several figures were made using the GMT software (Wessel and Smith, 1998). The GMSH Gnu software was used to build the models; meshes (gmsh.info).

Appendix A. Supplementary material

Supplementary material related to this article can be found online at https://doi.org/10.1016/j.epsl.2019.06.005.

References

Andersen, N.L., Singer, B., Jicha, B., Hildreth, E., Fierstein, J., Rogers, N., 2012. Evolution of rhyolite at Laguna del Maule, a rapidly inflating volcanic field in the Southern Andes. In: Proceedings of the Fall Meeting of Am. Geophys. Un. San Francisco, USA.

Andersen, N.L., Singer, B.S., Jicha, B.R., Beard, B.L., Johnson, C.M., Licciardi, J.M., 2017. Pleistocene to Holocene growth of a large upper crustal rhyolitic magma reservoir beneath the active laguna del Maule Volcanic field, Central Chile. J. Petrol. 58 (1), 85–114.

Annen, C., 2009. From plutons to magma chambers: thermal constraints on the accumulation of eruptible silicic magma in the upper crust. Earth Planet. Sci. Lett. 284 (3–4), 409–416.

Bonafede, M., Ferrari, C., 2009. Analytical models of deformation and residual gravity changes due to a Mogi source in a viscoelastic medium. Tectonophysics 471 (1–2), 4–13.

Cardona, C., Tassara, A., Gil Cruz, F., Lara, L.E., Morales, S., Kohler, P., Franco, L., 2018. Crustal seismicity associated to rapid uplift at Laguna del Maule volcanic complex, Southern Volcanic Zone of Andes. J. Volcanol. Geotherm. Res. https://doi.org/10.1016/j.jvolgeores.2018.01.009.

Cayol, V., Cornet, F.H., 1998. Effects of topography on the interpretation of the deformation field prominent volcanoes – application to Etna. Geophys. Res. Lett. 25, 1979–1982.

Cerpa, N.G., Araya, R., Gerbault, M., Hassani, R., 2015. Relationship between slab dip and topography segmentation in an oblique subduction zone: insights from numerical modeling. Geophys. Res. Lett. 42 (14), 5786–5795.

Charlier, B.L.A., Wilson, C.J.N., Lowenstern, J.B., Blake, S., Van Calsteren, P.W., Davidson, J.P., 2004. Magma generation at a large, hyperactive silicic volcano (Taupo, New Zealand) revealed by U–Th and U–Pb systematics in zircons. J. Petrol. 46 (1), 3–32.

Chéry, J., Zoback, M.D., Hassani, R., 2001. An integrated mechanical model of the San Andreas fault in central and northern California. J. Geophys. Res., Solid Earth 106 (B10), 22051–22066.

Contreras, M., Tassara, A., Gerbault, M., Araya, R., Bataille, K., 2016. Interseismic deformation at subduction zones investigated by 2D numerical modeling: case study before the 2010 Maule earthquake. Andean Geol. 43 (3), 247–262.

Cooper, K.M., Kent, A.J., 2014. Rapid remobilization of magmatic crystals kept in cold storage. Nature 506 (7489), 480.

Cordell, D., Unsworth, M., Diaz, D., 2018. Imaging the Laguna del Maule Volcanic Field, central Chile using magnetotellurics: evidence for crustal melt regions laterally-offset from surface vents and lava flows. Earth Planet. Sci. Lett. 488, 168–180.

Cundall, P.A., 1988. A microcomputer program for modeling large-strain plasticity problems. In: Numerical Methods in Geomechanics (Innsbruck 1988), pp. 2101–2108.

Currenti, G., Williams, C.A., 2014. Numerical modeling of deformation and stress fields around a magma chamber: constraints on failure conditions and rheology. Phys. Earth Planet. Inter. 226, 14–27.

Degruyter, W., Huber, C., 2014. A model for eruption frequency of upper crustal silicic magma chambers. Earth Planet. Sci. Lett. 403, 117–130.

Del Negro, C., Currenti, G., Scandura, D., 2008. Temperature-dependent viscoelastic modeling of ground deformation: application to Etna volcano during the 1993–1997 inflation period. Phys. Earth Planet. Inter. https://doi.org/10.1016/j.pepi.2008.1010.1019.

Dieterich, J.H., Decker, R.W., 1975. Finite element modelling of surface deformation associated with volcanism. J. Geophys. Res. 80 (29), 4094–4102.

Dragoni, M., Magnanensi, C., 1989. Displacement and stress produced by a pressurized, spherical magma chamber surrounded by a viscoelastic shell. Phys. Earth Planet. Inter. 56, 316–328.

Feigl, K., Le Mével, H., Tabrez Ali, S., Cordova, L., Andersen, N., DeMets, C., Singer, B., 2013. Rapid uplift in Laguna del Maule volcanic field of the Andean Southern Volcanic zone (Chile) 2007–2012. Geophys. J. Int. https://doi.org/10.1093/gji/ggt438.

Fournier, T.J., Pritchard, M.E., Riddick, S.N., 2010. Duration, magnitude, and frequency of subaerial volcano deformation events: new results from Latin America using InSAR and a global synthesis. Geochem. Geophys. Geosyst. 11 (1), Q01003.

Galetto, F., Acocella, V., Caricchi, L., 2017. Caldera resurgence driven by magma viscosity contrasts. Nat. Commun. 8 (1), 1750.

Gerbault, M., Hassani, R., Novoa Lizama, C., Souche, A., 2018. Three-dimensional failure patterns around an inflating magmatic chamber. Geochem. Geophys. Geosyst. 19 (3), 749–771.

Hassani, R., Jongmans, D., Chery, J., 1997. Study of plate deformation and stress in subduction processes using two-dimensional numerical models. J. Geophys. Res. 102 (B8), 17951–17965.

Hildreth, W., 2004. Volcanological perspectives on Long Valley, Mammoth Mountain, and Mono Craters: several contiguous but discrete systems. J. Volcanol. Geotherm. Res. 136 (3–4), 169–198.

Hildreth, W., Wilson, C.J., 2007. Compositional zoning of the Bishop Tuff. J. Petrol. 48 (5), 951–999.

Hildreth, W., Godoy, E., Fierstein, J., Singer, B., 2010. Laguna del Maule Volcanic field: eruptive history of a Quaternary basalt-to-rhyolite distributed volcanic field on the Andean range crest in central Chile. Serv. Nac. Geol. Min., Bol. 63. 142 pp.

Jellinek, M.A., DePaolo, D.J., 2003. A model for the origin of large silicic magma chambers: precursors of caldera-forming eruption. Bull. Volcanol. 65, 363–381.

Le Mével, H., Feigl, K., Cordova, L., DeMets, C., Lundgren, P., 2015. Evolution of unrest at Laguna del Maule volcanic field (Chile) from InSAR and GPS measurements, 2003 to 2014. Geophys. Res. Lett. 42 (16), 6590–6598.

Le Mével, H., Gregg, P.M., Feigl, K., 2016. Magma injection into a long-lived reservoir to explain geodetically measured uplift: application to the 2007–2014 unrest episode at Laguna del Maule volcanic field, Chile. J. Geophys. Res., Solid Earth 121 (8), 6092–6108.

Levenberg, K., 1944. A method for the solution of certain non-linear problems in least squares. Q. Appl. Math. 2 (2), 164–168.

Mastelark, T., 2007. Magma intrusion and deformation predictions: sensitivities to the Mogi assumptions. J. Geophys. Res., Solid Earth 112 (B6).

Miller, C.A., Williams-Jones, G., Fournier, D., Witter, J., 2017. 3D gravity inversion and thermodynamic modelling reveal properties of shallow silicic magma reservoir beneath Laguna del Maule, Chile. Earth Planet. Sci. Lett. 459, 14–27.

Newman, A.V., Dixon, T.H., Ofoegbu, G.I., Dixon, J.E., 2001. Geodetic and seismic constraints on recent activity at Long Valley Caldera, California: evidence for viscoelastic rheology. J. Volcanol. Geotherm. Res. 105 (3), 183–206.

Newman, A.V., Dixon, T.H., Gourmelen, N., 2006. A four-dimensional viscoelastic deformation model for Long Valley Caldera, California, between 1995 and 2000. J. Volcanol. Geotherm. Res. 150, 244–269.

Okada, Y., 1985. Surface deformation due to shear and tensile faults in a half-space. Bull. Seismol. Soc. Am. 75, 1135–1154.

Parks, M.M., Moore, J.D., Papanikolaou, X., Biggs, J., Mather, T.A., Pyle, D.M., et al., 2015. From quiescence to unrest: 20 years of satellite geodetic measurements at Santorini volcano, Greece. J. Geophys. Res., Solid Earth 120 (2), 1309–1328.

Pascal, K., Neuberg, J., Rivalta, E., 2013. On precisely modelling surface deformation due to interacting magma chambers and dykes. Geophys. J. Int. 196 (1), 253–278.

Perfettini, H., Avouac, J.P., Tavera, H., Kositsky, A., Nocquet, J.M., Bondoux, F., Chlieh, M., Sladen, A., Audin, L., Farber, D., Soler, P., 2010. Seismic and aseismic slip on the Central Peru megathrust. Nature 465 (7294), 78–81.

Pritchard, M.E., Mather, T.A., McNutt, S.R., Delgado, F.J., Reath, K., 2019. Thoughts on the criteria to determine the origin of volcanic unrest as magmatic or nonmagmatic. Philos. Trans. R. Soc. Lond. A 377 (2139), 20180008.

Remy, D., Froger, J.L., Perfettini, H., Bonvalot, S., Gabalda, G., Albino, F., Cayol, V., Legrand, D., Saint Blanquat, M.D., 2014. Persistent uplift of the Lazufre volcanic complex (Central Andes): new insights from PCAIM inversion of InSAR time series and GPS data. Geochem. Geophys. Geosyst. 15 (9), 3591–3611.

Rubin Allan, M., 1995. Getting granite dikes out of the source region. J. Geophys. Res., Solid Earth 100 (B4), 5911–5929.

Sambridge, M., 1999a. Geophysical inversion with a neighbourhood algorithm, I: appraising the ensemble. Geophys. J. Int. 138, 727–746.

Sambridge, M., 1999b. Geophysical inversion with a neighbourhood algorithm, II: searching a parameter space. Geophys. J. Int. 138, 479–494.

Segall, P., 2010. Earthquake and Volcano Deformation. Princeton University Press.

Segall, P., 2016. Repressurization following eruption from a magma chamber with a viscoelastic aureole. J. Geophys. Res., Solid Earth 121 (12), 8501–8522.

Segall, P., 2019. Magma chambers: what we can, and cannot, learn from volcano geodesy. Philos. Trans. R. Soc. A 377, 20180158.

Singer, B.S., Andersen, N.L., Le Mével, H., Feigl, K.L., DeMets, C., Tikoff, B., Thurber, C., Jicha, B., Cardona, C., Cordova, L., Gil, F., Unsworth, M., Williams-Jone, G., Hildreth, W., Fierstein, J., Vaszquez, J., 2014. Dynamics of a large, restless, rhyolitic magma system Laguna del Maule, southern Andes, Chile. GSA Today 24 (2), 4–10.

Singer, B.S., Le Mével, H.l.n., Licciardi, J.M., Cordova, L., Tikoff, B., Garibaldi, N., Andersen, N.L., Diefenbach, A.K., Feigl, K.L., 2018. Geomorphic expression of rapid Holocene silicic magma reservoir growth beneath Laguna del Maule, Chile. Sci. Adv. 4 (6).

Szymanowski, D., Wotzlaw, J.r.-F., Ellis, B.S., Bachmann, O., Guillong, M., von Quadt, A., 2017. Protracted near-solidus storage and pre-eruptive rejuvenation of large magma reservoirs. Nat. Geosci. 10, 777.

Townsend, M., Huber, C., Degruyter, W., Bachmann, O., 2019. Magma chamber growth during inter-caldera periods: insights from thermo-mechanical modeling with applications to Laguna del Maule, Campi Flegrei, Santorini, and ASO. Geochem. Geophys. Geosyst.

Wagner, V.R., Diaz, D., Darcy, C., Unsworth, M., 2017. Regional electrical structure of the Andean subduction zone in central Chile (35°–36°S) using magnetotellurics. Earth Planets Space. https://doi.org/10.1186/s40623-017-0726-z.

Wessel, P., Smith, W.H., 1998. New, improved version of Generic Mapping Tools released. Eos Trans. AGU 79 (47), 579.

Supplementary Material for: Viscoelastic relaxation: a mechanism to explain the decennial large surface displacements at Laguna del Maule silicic volcanic complex

Novoa C., Remy D., Gerbault M., Baez J.C, Tassara A.,
Cordova L., Cardona C., Granger M, Bonvalot S., Delgado F.

May 29, 2019

The Supplement contains:

- Supplementary Text: S1 to S5
- Supplementary Figures: S1 to S21
- Supplementary Tables: S1 to S2

Introduction

Section S1 presents in details GNSS and InSAR processing used in this study. Section S2.1 presents a principal component analysis based on singular value decomposition and Section S2.2 details the strategy adopted to determine the easting and vertical displacement maps from ascending and descending Sentinel-1 data. Section S3 presents modeled ground surface displacement using classical analytical models. Section S4 presents a benchmark between the analytical solutions of Dragoni et al. (1989) and the numerical solutions obtained with the 3D finite-element code ADELI, for a viscoelastic rheology in an infinite medium. S4 presents another comparison between the numerical solutions of ADELI and those by Segall (2010), accounting for a free surface. Section S5 presents the comparison of surface displacement patterns between a pressurized elliptical source immersed in an elastic medium and a small pressurized source surrounded by a viscoelastic shell. In this section we show that the viscoelastic model reproduces the surface displacements produced by the elastic model after a period of time.

S1 GNSS and InSAR processing

S1.1 GNSS data

Ground deformation at LdM was characterized from daily solutions at five continuous GNSS stations installed by the Observatorio Volcanológico de los Andes del Sur (OVDAS) covering a period of about five years (May 2012 to April 2017). The GNSS data were provided by OVDAS and processed using the GIPSY software from JPL. We obtained the precise ground displacement time series in three dimensions at GNSS stations after correcting for plate motion and long spatial wavelength post-seismic surface deformation associated with the 2010 Maule earthquake derived from the data recorded at MAUL station, about 39 km away from the center of the LdM volcanic complex (Li et al., 2018). The 1σ accuracy of the daily station positions is estimated at 3 mm and 5 mm for the horizontal and the vertical components, respectively.

S1.2 InSAR data

SAR imagery over LdM was acquired by two satellite missions: C-band Interferometric Wide Swath mode images from the European Space Agency (ESA) Sentinel-1A/B and L-band Stripmap mode images from ALOS 1 and 2 operated by the Japan Aerospace Exploration Agency (JAXA). The C-band SAR dataset (Table 1) includes 33 acquisitions from ascending orbits (6 October 2014 to January 2017), and 32 acquisitions from descending orbits (23 October 2014 to 23 March 2017). The L-band SAR dataset is composed of 17 PALSAR images from ascending orbits (26 January 2007 to 8 January 2011) and 5 PALSAR-2 images from descending orbits (12 March 2015 to 4 May 2017).

We used the DIAPASON software (Diapason, 2006) to generate the differential interferograms, using the two-pass method described by Massonnet and Feigl (1995). For Sentinel data, we used the 3 arcsec Shuttle Radar Topographic Mission digital elevation model (SRTM) to remove the topographic contribution and the 1 arcsec SRTM for the other SAR data. We used the 1 arcsec SRTM to provide a geographic framework (UTM WGS84) for the interferograms. The criteria used for selecting data were, to have a perpendicular baseline lower than 1500 m, and that for the ALOS-2 and Sentinel 1 satellites orbital with separations not exceeding 200 m, no selection was taken into account.

Next, a weighted power spectral density filter (Goldstein et al., 1988) was used to filter the interferograms which were later unwrapped using an implementation of the Statistical cost, Network- flow Algorithm for Phase Unwrapping -SNAPHU (Chen and Zebker, 2002). The resulting interferograms indicate large seasonal variation in coherence with a strong decrease

during the austral winter. This leads us to disregard interferograms computed with a pair of images acquired during the winter season for our ground deformation analysis. The resulting high-coherent interferogram dataset was next unwrapped using the SNAPHU Algorithm.

Many interferograms reveal large-wavelength phase signals or phase signal varying with topography. As the magnitude of these signals is not correlated with the Perpendicular baseline, we considered that they are produced either by a change in variation of water vapor or by a pressure change. To mitigate the phase delays we corrected the interferograms using a simple empirical function that correlates phase and topography and a ramp function (linear function and a phase offset) to account for long wavelength signals after masking the area affected by displacements (see Remy et al., 2014 for more details). This step also enables us to estimate the uncertainty for each interferogram and to make phase values comparable in both space and time.

S2 Time Series Analysis

S2.1 Principal component analysis using Singular Value Decomposition

GNSS and InSAR time series are decomposed separately into the sum of its principal components:

$$X_{svd} = \sum_{k=1}^{n_{comp}} U_k S_k V_k^t$$

where U,S, and V are the spatial function matrix, the matrix of the principal values and the time function matrix. Whatever the time series considered the resulting first component explains 82% and about 70% of the total variation in the surface displacements for the GNSS (horizontal and vertical) and InSAR (LOS) data respectively, followed by a 5% to 3% of the total variation explained by the second component, confirming that most information is contained in the first component (Figure S1).

The resulting time functions of the first component of all the dataset show a similar linear temporal behaviour related to the on-going uplift. The first spatial functions of the InSAR time series reveal an elliptical displacement pattern which only differ according to their satellite viewing geometry. The amplitude of these first spatial components is much greater than those of the second and third components, clearly indicating that this elliptical displacement pattern is the dominant feature in the InSAR time series. To determine how well the data are represented by the different components we computed the reduced Chi square of the residual of the data for the 1 to k-th components.

$$\chi_r^2 = \frac{1}{N-k} \sum \left[\frac{X - X_{svd}}{\sigma} \right]^2$$

where N refers to the number of GNSS or InSAR data , k is the number of principal components selected for the signal reconstruction, X is the data matrix, X_{svd} is the reconstructed data matrix obtained by multiplying the k spatial components by their respective singular values and time functions, and σ is the data standard error.

χ_r^2 of the residuals between the observed and the reconstructed time series for the first component are 1 for GNSS and 0.3, 0.28 and 0.25 for ALOS-2, Sentinel-1 ascending track and descending track, respectively (Figures 2 of the main text and S2). The low values of χ_r^2 for InSAR data indicate that 1) the reconstructed time series using the first component lie within the data uncertainty and 2) that our estimation of the InSAR data uncertainty seems a little bit overestimated. Taking into account this low value of χ_r^2 and the fact that the residuals between the observed and the reconstructed data do not reveal a clear pattern of coherent misfits over time, we consider that high-order components are negligible to reconstruct the observed signal. Nevertheless, the higher value of χ_r^2 for the GNSS data set could indicate that ground displacement could be driven by more than one process.

As we suspect that a major part of the variance in GNSS data set is due to seasonal vertical signals, we decompose separately the horizontal and the vertical components of the displacements. The resulting χ_r^2 between the original data and the reconstructed one are 0.7 and 1.05 for the horizontal and the vertical components, showing that seasonal vertical signals recorded at the GNSS stations produce the major part of the variance signal not explained by the first component of the decomposition. All these results lead to the conclusion that the spatial pattern of the displacement did not change significantly during the three-year period (Oct. 2014 - Jul 2017), and that the amplitude of these displacements described by the first temporal function of InSAR and GNSS data decompositions evolves linearly over time.

S2.2 Easting and vertical displacement maps at LdM

We benefit from the ascending and descending Sentinel-1 tracks to retrieve the easting and the vertical components of the ground displacement, allowing us to map the displacement field at LdM. We consider only Sentinel data because they cover a period longer than the one covered by ALOS-2 data. Due to the near-polar orbit of Sentinel satellites, we do not take into account the northing component as it is poorly constrained. We assume here (taking GNSS measurement into account) that the northing displacements are not higher in magnitude than the vertical and the east components since they essentially vanish when they are projected in the radar line of sight. In order to make ascending and descending Sentinel InSAR displacements compatible

in time, we select the overlapping period and we use linear interpolation at missing epochs in time.The displacement rates in the 2D components of the ground displacement is finally inverted based on the vectors pointing from the ground to the satellite LOS and using the approach proposed by Wright et al. (2004).

S3 Analytical models

In this section, we consider a variety of classical analytical source models (a Mogi-type point source, a spheroidal Yang-type source and an Okada-type dislocation) to model surface displacement at LdM. Inversions favor flat-topped sources rather than spheres or prolate ellipsoids (see Table S1) in agreement with what is expected from the ratio of maximum horizontal to maximum vertical displacement, equal to about 0.31 according to the GNSS data [Dieterich and Decker, 1975 ; Fialko et al., 2001 ; Fialko and Pearse, 2012 ; Remy et al., 2014]. This result is also in agreement with the assumption that the observed uplift at LdM could be produced by a sill intrusion at about 5 km depth below the surface [Fournier et al., 2010 ; Feigl et al., 2013; Le Mével et al., 2015].

Figure S3 shows the displacement observed on the largest period of each track and on a three-year 2014-2017 period of GNSS data, the modeled displacements using Okada-type displocation with the smallest misfit and the resulting residual between the observed and the modeled displacements. This model fails to properly match the GNSS data yielding χ^2_rr of about 8.5 (Figure S3.B). This high value of χ^2_r is mainly associated with significant differences between the observed horizontal displacements observed by GNSS and those modeled. We observe the same behavior from InSAR data. The model matches well the entire InSAR dataset when each tracks are inverted separately ($\chi^2_r = 0.75$), but the location of the center of this source differs according to each specific track. The inversion of the ascending tracks alone leads to the estimation of a center 1.5 km further to the west with respect to the inversion of the descending tracks. Consequently, the combined inversion using Sentinel and ALOS-2 data leads to an increase of χ^2_r between the value predicted by the model and the data. Although this model yields χ^2_r for the InSAR data close to 1, this value increases with the time span between a given InSAR time series map and the reference image used for the least square adjustment, due to the presence of localized residual patterns located around the lake.

S4 Benchmark of Adeli-3D with viscoelastic analytical solutions

To evaluate the accuracy of Adeli-3D in simulating a viscoelastic rheology, we benchmark its numerical solutions with analytical solutions of surface displacements due to the pressurization of a spherical source surrounded by a Maxwell viscoelastic spherical shell. First, we present the analytical solutions of Dragoni et al. (1989), in which an infinite space domain is assumed (IDM). Second, we present the analytical solutions provided by Segall (2010) for a half-space domain HDM).

In order to estimate the differences between analytical and numerical solutions, we calculate the maximum local discrepancies $\epsilon|_{max}$, Eq.1, that correspond to the normalized difference at the maximum of the analytical (U_x^{An}) and numerical surface displacement (U_x^{FE}), following Pascal et al. (2013):

$$\epsilon|_{max} = \frac{abs\left\{U_x^{An}|_{max} - U_x^{FE}|_{max}\right\}}{abs\{U_x^{An}|_{max}\}} \tag{1}$$

S4.1 A visco-elastic shell in an infinite domain

Dragoni et al. (1989) assumed an Infinite Domain Model (IDM); this model provides analytical solutions for radial displacements (u_r) due to a trapezoidal pressure history in a spherical source surrounded by a concentric, spherical, Maxwell viscoelastic shell (Eq. 2).

$$u_r(r,t) = \frac{1}{4}\frac{P_0}{G}\frac{R_2^3}{r^2}\left[f_1(t) - \left(1 - \frac{R_1^3}{R_2^3}\right)f_2(t)\right]. \tag{2}$$

Where r is the distance between the center of the magmatic source and a point outside the source, P_0 is the applied pressure, G is the shear modulus, R_1 is the radius of the magmatic source, η is the viscosity in the shell and R_2 is the radius of the larger viscoelastic shell. Other variables are :

$$f_1(t) = \frac{t - (t-t_1)H(t-t_1)}{t_1} + \frac{(t-t_3)H(t-t_3) - (t-t_2)H(t-t_2)}{t_3 - t_2},$$

$$f_2(t) = \tau\left(\frac{M-N}{t_1} + \frac{O-P}{t_3-t_2}\right),$$

$$M = 1 - e^{\frac{-t}{\tau}}, \qquad N = H(t-t_1)(1 - e^{\frac{-(t-t_1)}{\tau}}),$$

$$O = H(t-t_3)(1 - e^{-\frac{(t-t_3)}{\tau}}), \;\; P = H(t-t_2)(1 - e^{-\frac{(t-t_2)}{\tau}}).$$

In the trapezoidal pressure history, the pressure increases linearly until t_1, then remains constant until t_2, and decreases linearly to zero until t_3. H(t) is the Heaviside step function ($H = 1$ when $t > 0$ and $H = 0$ when $t < 0$), and the characteristic time τ depends not only on η and G, but also on the dimensions of the shell:

$$\tau = \frac{9}{5}\frac{\eta}{G}\left(\frac{R_2}{R_1}\right)^3.$$

.

S4.2 A visco-elastic shell in a half-space domain

Segall (2010) provides an approximate solution for the vertical displacements (u_z) at the free-surface due to an instantaneous increase of magma pressure in a spherical source, surrounded by a Maxwell viscoelastic spherical shell, immersed in a half-space domain (Eq. 3).

$$u_z(\rho, z = 0, t) = \frac{(1-\nu)p_0 R_1^3}{\mu d^2}\left[e^{-t/t_R} + \frac{R_2^3}{R_1^3}(1 - e^{-t/t_R})\right]\frac{1}{(1+\rho^2)^{3/2}} \quad (3)$$

with,

$$t_R = \frac{3\eta(1-\nu)R_2^3}{\mu(1+\nu)R_1^3}$$

where ρ is the radial distance from the center of the source normalized by the source depth, p_0 is the instantaneous pressure acting at the walls of the spherical source, ν the Poisson's ratio, R_1 is the radius of the magmatic source, R_2 is the radius of the shell, μ the shear modulus, d is the depth to the center of the source, t is time, t_R is the characteristic relaxation time and η is the viscosity.

S4.3 Infinite Domain Model (IDM) and Half Space Model (HSM)

First, we compare the surface displacements obtained by the analytical solutions of Dragoni et al. (1989) assuming an Infinite Domain model (IDM) with the numerical solutions of Adeli-3D. These surface displacements are produced by a spherical pressurized source surrounded by a concentric spherical Maxwell viscoelastic shell. The applied pressure has a trapezoidal time variation and the surface displacements are calculated at a radial distance of 6 km from the source's center.

In order to bench Dragoni's model, we simulate an IDM with a box of size 80 [km] x 80 [km] x 80 [km] in which a chamber is located at its center (at 40 km depth, Fig.S4). We bench Dragoni's model in Fig. S5. Our numerical results show the impact of the mesh resolution on the magnitude of surface displacement, reaching a maximum local discrepancy of $\epsilon|_{max} = 25\%$ for a mesh resolution of 300 [m], then decreasing for a resolution of 100 [m], Fig.S6a. The numerical surface displacements corresponding to the analytical solutions proposed by Dragoni and Magnanensi et al. (1989) were reached for a numerical model with resolution of 100 m, including a high resolution (100 [m]) square domain situated 6 km above and below the source ($\epsilon|_{max} = 0.5$ %).
Furthermore, we evaluate the numerical temporal resolution necessary to calibrate our numerical solutions with the analytical solutions. Fig.S6b shows that we obtain a solution with $\epsilon|_{max} = 0.5\%$ when using 87500 numerical time steps, or more.

Second, we compare the analytical solutions of Segall (2010) assuming a Half-Space model (HSM), with the numerical solutions of Adeli-3D. As in the first case, these surface displacements are produced by a spherical pressurized source surrounded by a concentric spherical Maxwell viscoelastic shell, but in this case we consider the free-surface condition.

In order to bench Segall's model, we use the same model box of size 80 [km] x 80 [km] x 80 [km], but we move the chamber to 6 km depth, leaving the upper surface free and considering a resolution of 100 [m] at the measurement points, Fig. S7 (box inside the large domain). In figure S8, we bench the figure 7.38 presented p.246 of Segall (2010), considering the vertical displacements of Eq. 3 normalized by $(1-\nu)p_0R_1^3/\mu d^2$. Fig. S8a displays the vertical displacement as a function of radial distance along the free surface at four different nondimensional times for the analytical solutions and for Adeli's numerical solutions. Fig. S8b shows the displacement as a function of nondimensional time immediately above the magma chamber for the analytical solutions and for Adeli's numerical solutions. For these models $R_2/R_1 = 1.2$.

As mentioned above, our results are displayed Fig.S5 and S8. We bench Dragoni's IDM model with Adeli 3D to $\epsilon|_{max} = 0.5$ %, and benchmark Segall's model to $\epsilon|_{max} = 1.11$ %. The local maximum discrepancies of these two models demonstrate that the differences in surface displacements provided by Adeli's numerical solutions are insignificant, since they are lower than 5% (Pascal et al., 2013).

S5 Comparing Surface displacements between viscoelastic and elastic models

In this section, we compare the spatial pattern of surface displacement due to: a) a large elliptical source of 100 km^3 pressurized with 10 [MPa] immersed in an elastic domain; and b) a small source of 10 km^3 pressurized with 10 [MPa] surrounded by a viscoelastic shell, itself immersed in an elastic domain. In this case the viscoelastic shell has the same geometry as the large elliptical source of case a). We use 'Elastic source' to refer to the first case and 'Viscoelastic source' to refer to the second case.

The 'Elastic source' model is illustrated in Fig.S9a. The surface displacements produced by the overpressure within this source were calculated using the BEM model (MC3, explained in section 3.3 of the main text). For the 'Viscoelastic source', the configuration of the source is illustrated in Fig.S9b. In this case, the surface displacements produced by the presurization of the small source were calculated using Adeli-3D, counting for the viscoelastic response of the shell. Considering the temporal evolution inherent to a viscoelastic behavior, this second model was ran for 10 [years], applying a linear increase of pressure from 0 to 10 [MPa] during the first year, and then the pressure remained constant for the next 9 years.

For the 'Viscoelastic source', our results show that the surface displacements continue to increase after the first year, Fig.S10 and Fig.S11, and evolve until the pressure is completely transfered to the shell's walls. We can see in Fig.S10 and S12 that after that, the surface displacements pattern is very close to that produced by the 'Elastic source'. In Fig.S13, Fig.S14 and Fig.S15, we compare surface displacements at the top-free surface produced by the 'Elastic source' and by the 'Viscoelastic source' after 10 years. The maximum local discrepancies between the elastic and viscoelastic assumptions are $\epsilon_{east}|_{max}$=2.0%, $\epsilon_{north}|_{max}$=0.7% and $\epsilon_{up}|_{max}$=1.0%, showing that the differences between the elastic and viscoelastic configurations are insignificant (Pascal et al., 2013).

These results show that it is possible to obtain surface displacements of the order of 1 [m] with a large pressurized source immersed in an elastic medium, but also with a viscoelastic shell surrounding a pressurized source of significant lower volume. The viscoelastic response of such a shell can contribute for 60 % of the surface displacements after the injection of new

magma.

Supplemental Figures

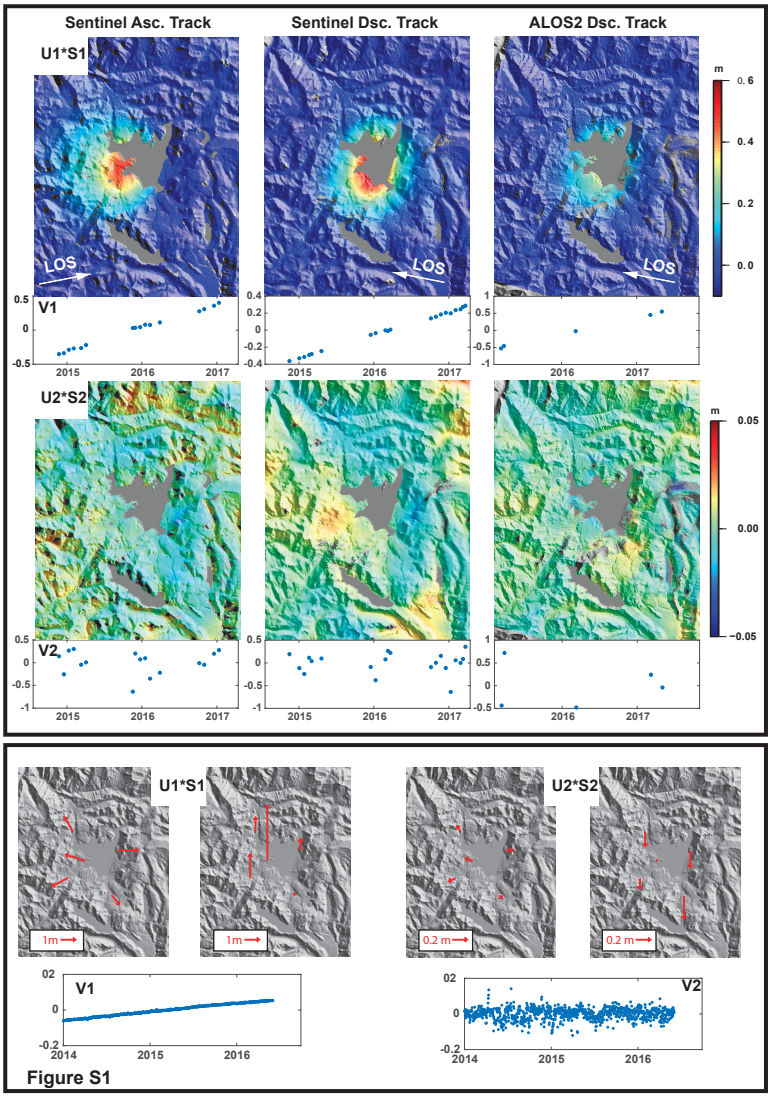

Figure S1: Results from the principal component decomposition applied to InSAR and GNSS time series. A) The first and the second spatial and temporal functions obtained for the three different tracks. They show the signal related to the inflation as observed with different viewing angles. The first component explains about 70% of the variance observed in InSAR data. The linear combination of the first component U1, S1 and V1 makes it possible to reconstruct the observed signal within the InSAR uncertainties whatever the track considered. B) The two first components of the GNSS time series. The first component explains 82% of the total variation in the surface displacements recorded at the GNSS stations. The first time function of each data set evolves linearly with time.

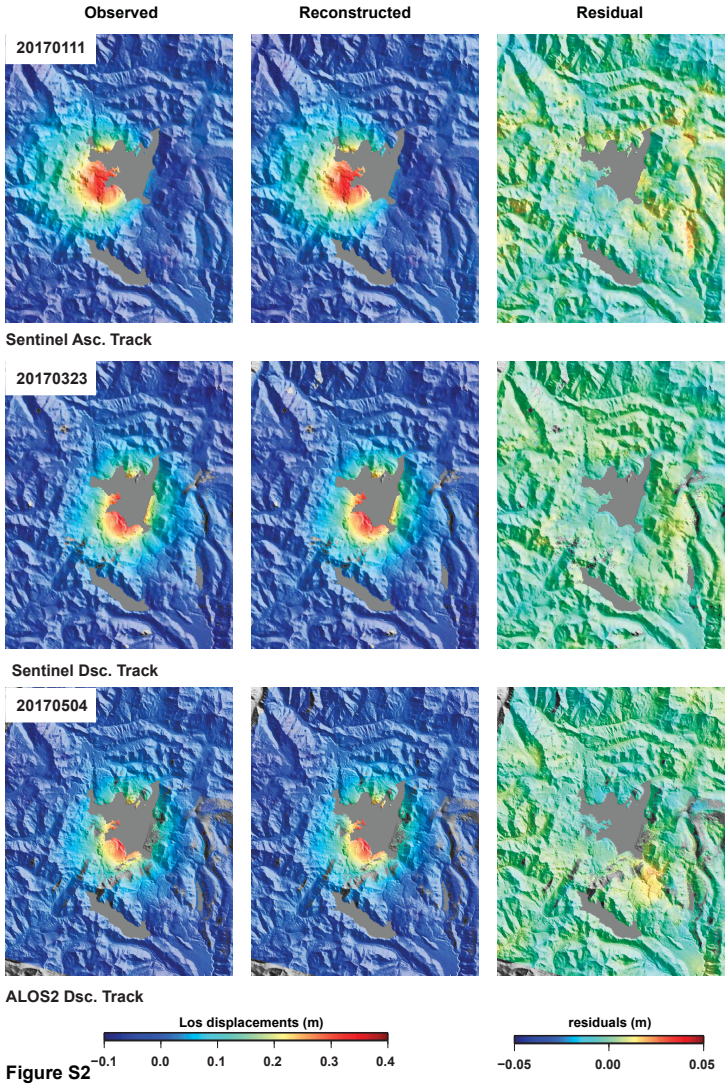

Figure S2: Examples of reconstructed displacements over LdM using the first principal component of the decomposition. Up) Adjusted LOS Displacement maps, Reconstructed LOS displacement maps using the first component of the decomposition and residual of the difference for the Sentinel ascending track. Middle) Same as previously but for the Sentinel descending track. Bottom) Same as previously, but for the ALOS descending track.

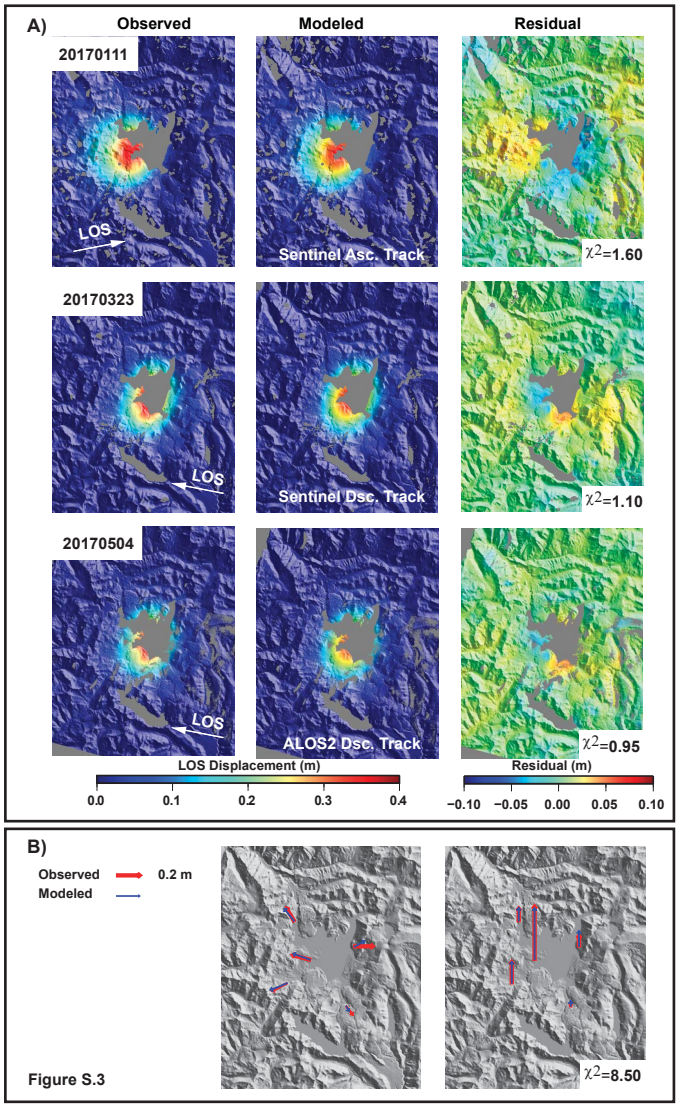

Figure S3: Maps of the observed and modeled GNSS and InSAR data using the best Okada-type dislocation. A) Upper, middle and botton include an example of three LOS displacement maps, the model prediction and the residuals between observed and modeled data. B) Observed cumulated horizontal and vertical GPS displacements (red vectors) from 2014 to 2017 and modeled displacements (blue vectors).

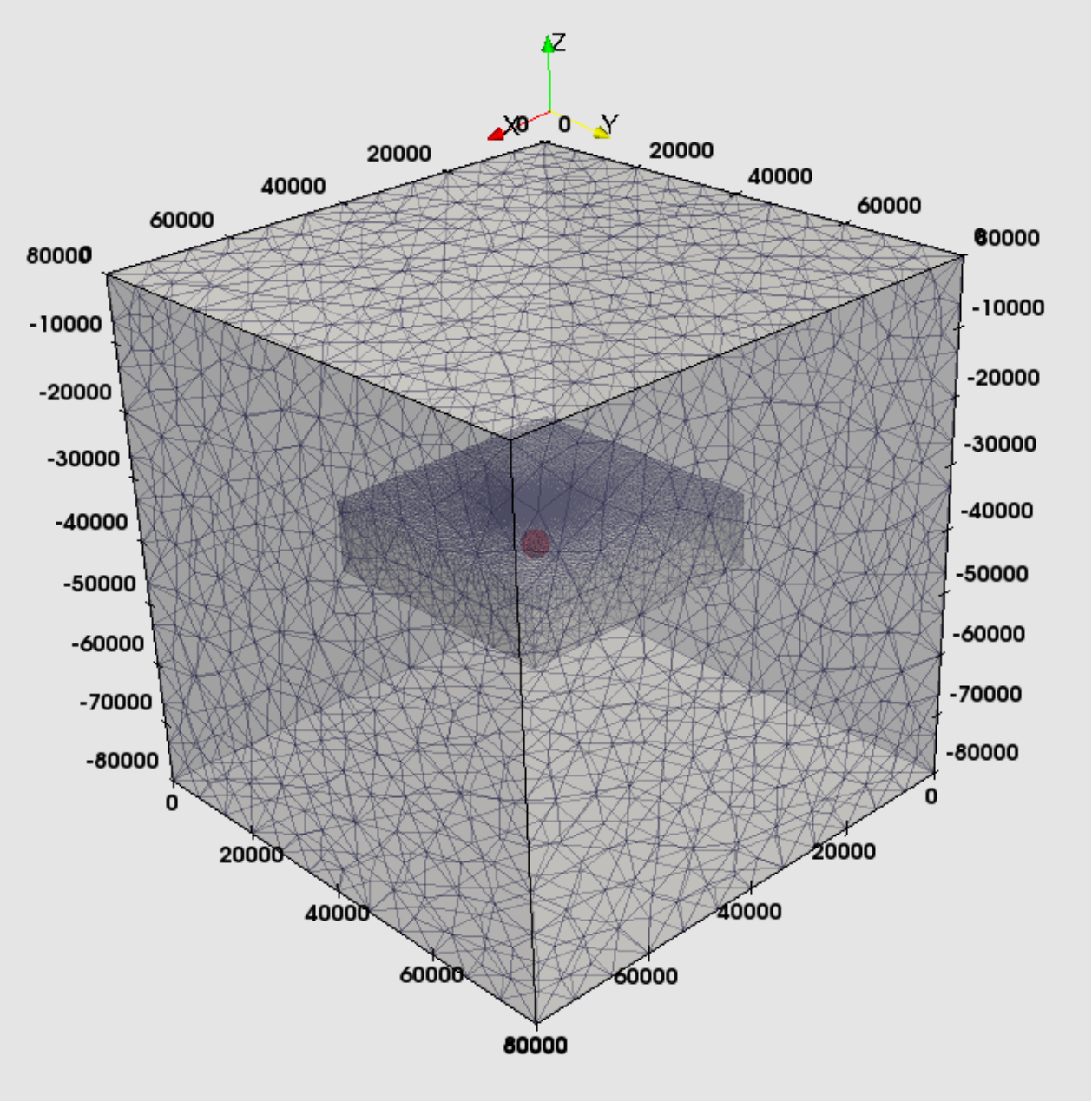

Figure S4: Mesh resolution used in S4.2, for Dragoni's model. The IDM was represented by a box of 80[km] x 80[km] x 80 [km]. The spherical source surrounded by the concentrical viscoelastic shell is located at -40000[m]. Into this domain we include a smaller box with high resolution surrounding the source. The upper boundary of this box is located 6000[m] above the source and its lower boundary is located 6000[m] below the source.

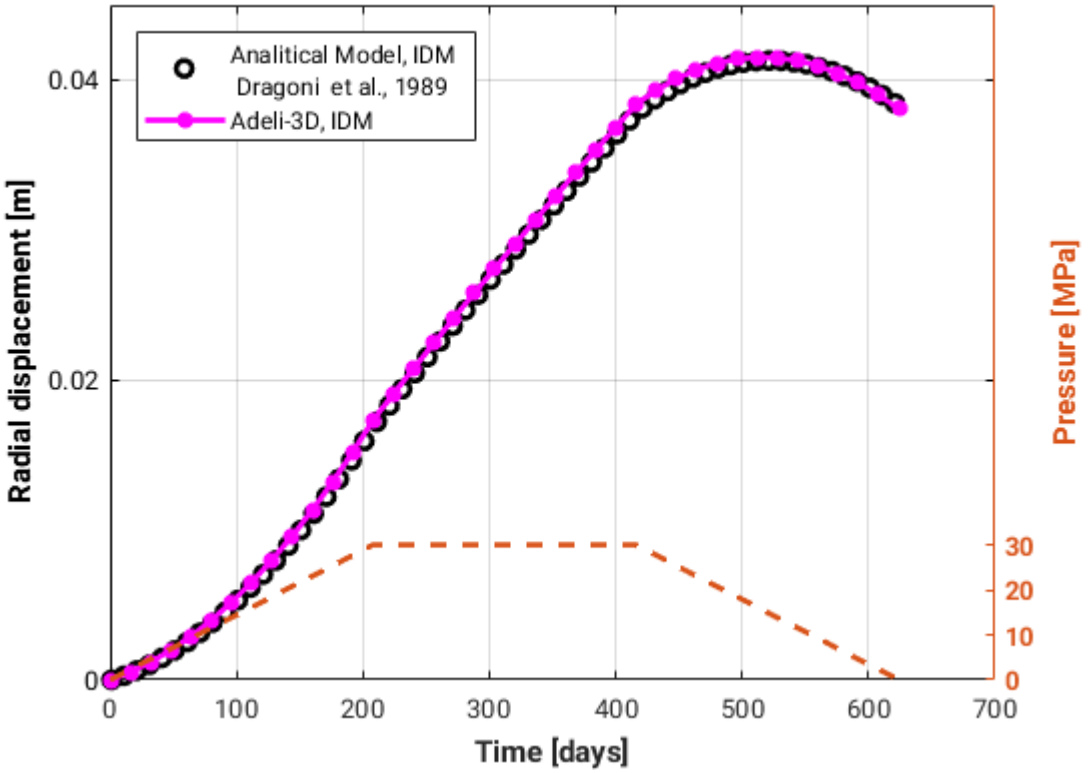

Figure S5: Predicted surface displacement produced by a trapezoidal time variation of pressure at a radial distance of 6 km between the source's center and the point of measure. Surface displacements were calculated using Dragoni's model assuming an IDM., and serve as a benchmark to validate the solutions calculated with Adeli 3D using Maxwell viscoelastiity.

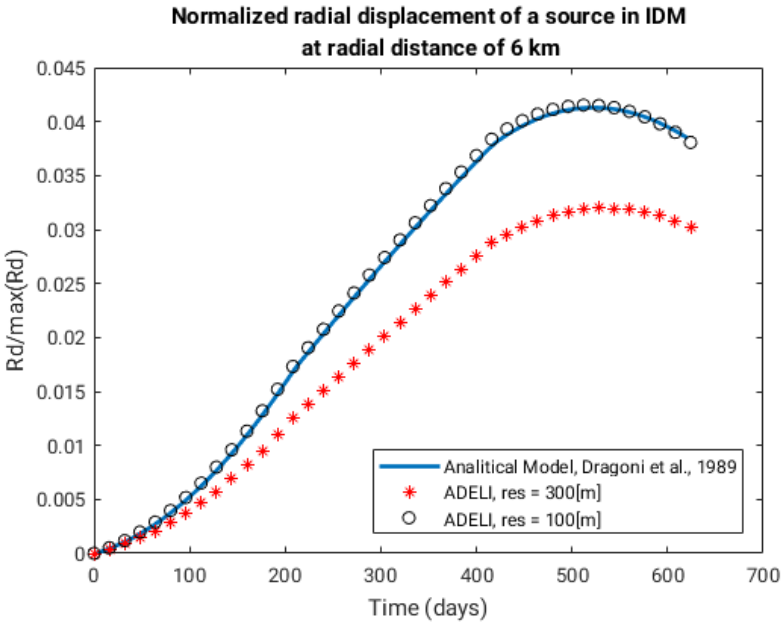

a)

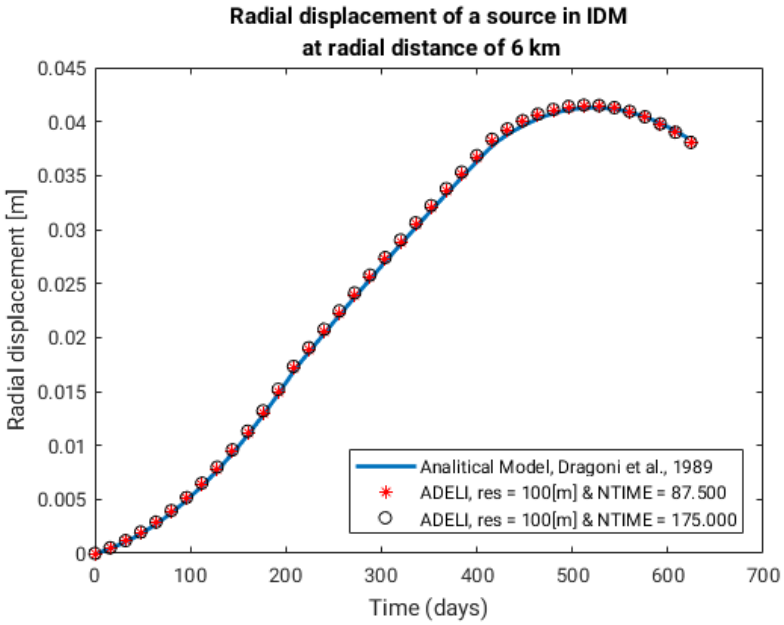

b)

Figure S6: Radial displacement produced by a source of radial distance 6 km immersed in an IDM. a) The resolution test shows that the numerical solution converges with the analytical solution of Dragoni et al., 1989 for a mesh resolution of 100[m]. The resolution test at 300[m] underestimates the surface displacement. b) Tests with different numerical time-steps ((iterations). A total number of time steps of 87500 and 175000 provide the same solution that converges to Dragoni's model.

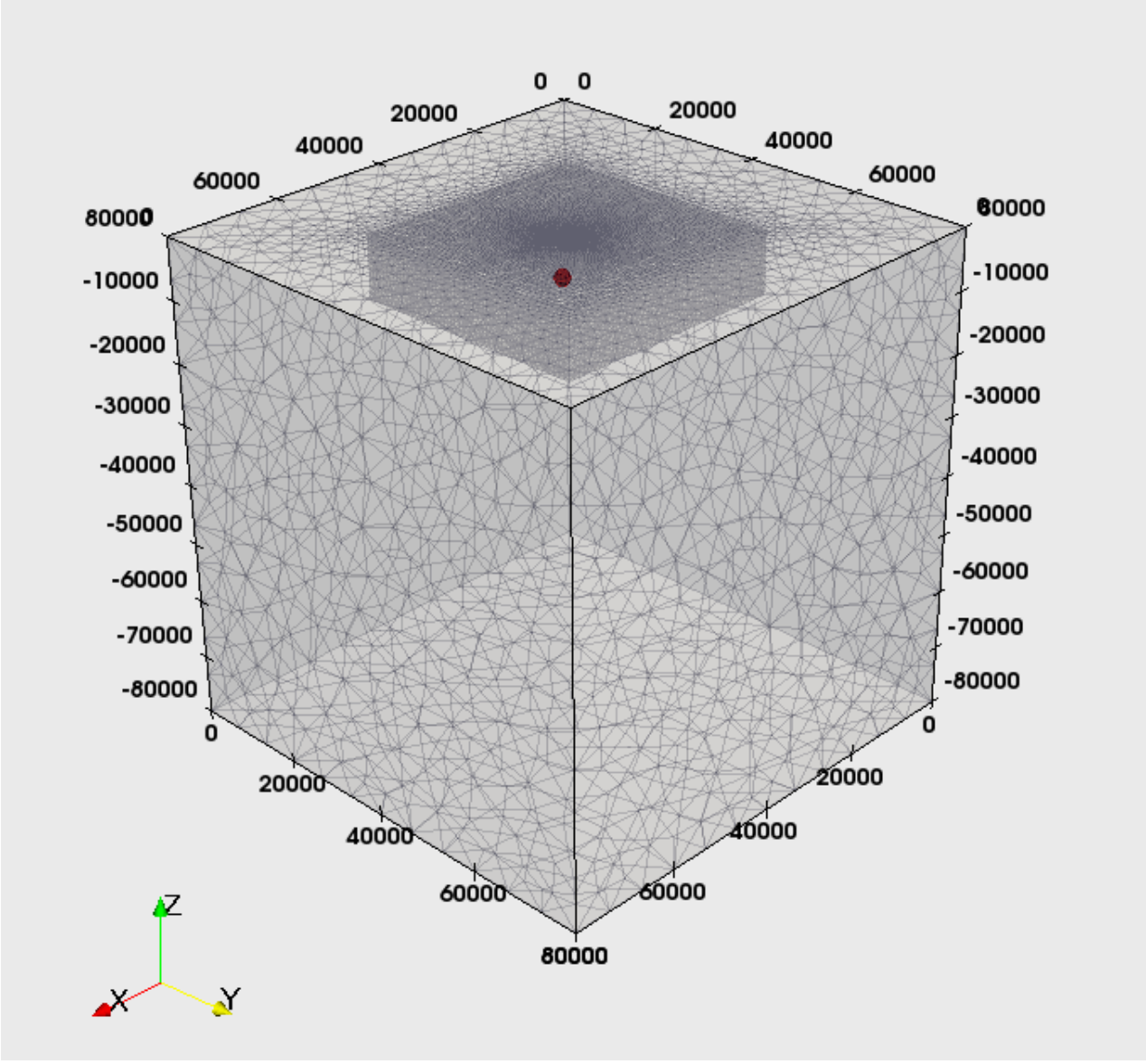

Figure S7: Mesh resolution used in S4.2, to bench Segall's model. The spherical source surrounded by a concentric viscoelastic shell is located at -6000[m]. The upper surface is set free (HSM definition). A smaller box of high resolution is also defined 6 km above the source.

a)

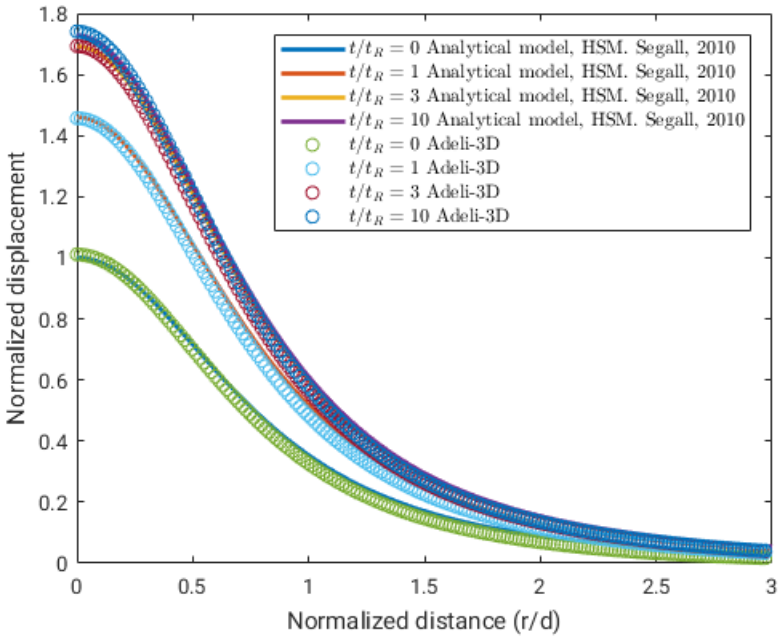

b)

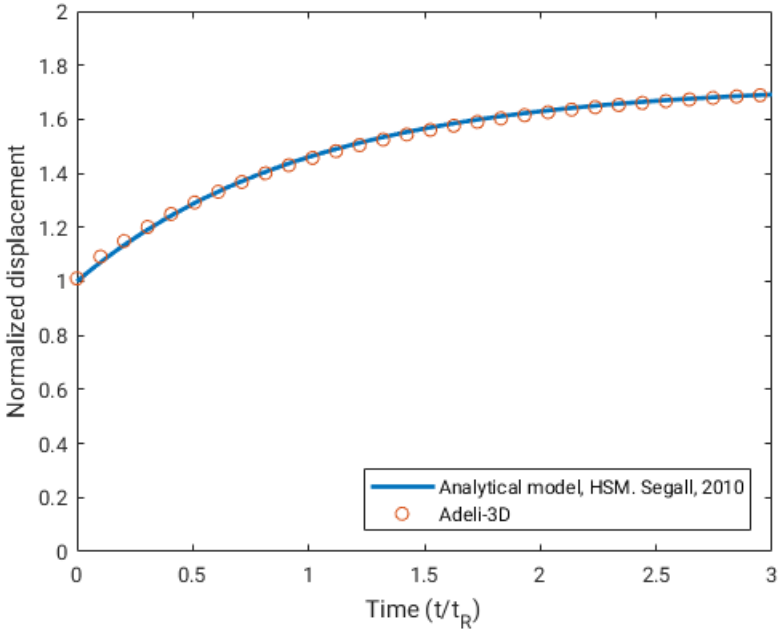

Figure S8: Figure modified from Segall et al. (2010). Numerical solutions using Adeli-3D and analytical solutions by Segall et al. (2010). Top figure: vertical displacement as a function of radial distance along the free surface at four nondimensional times. Bottom figure: displacement as a function of nondimensional time immediately above the magma chamber.

a)

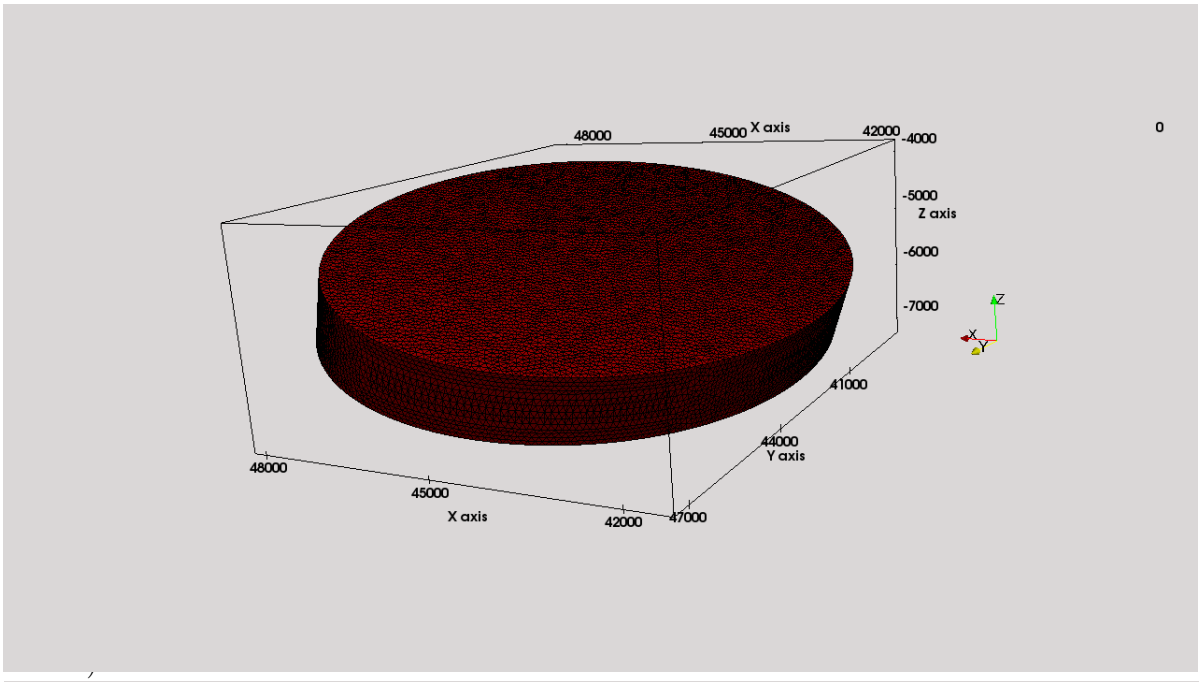

b)

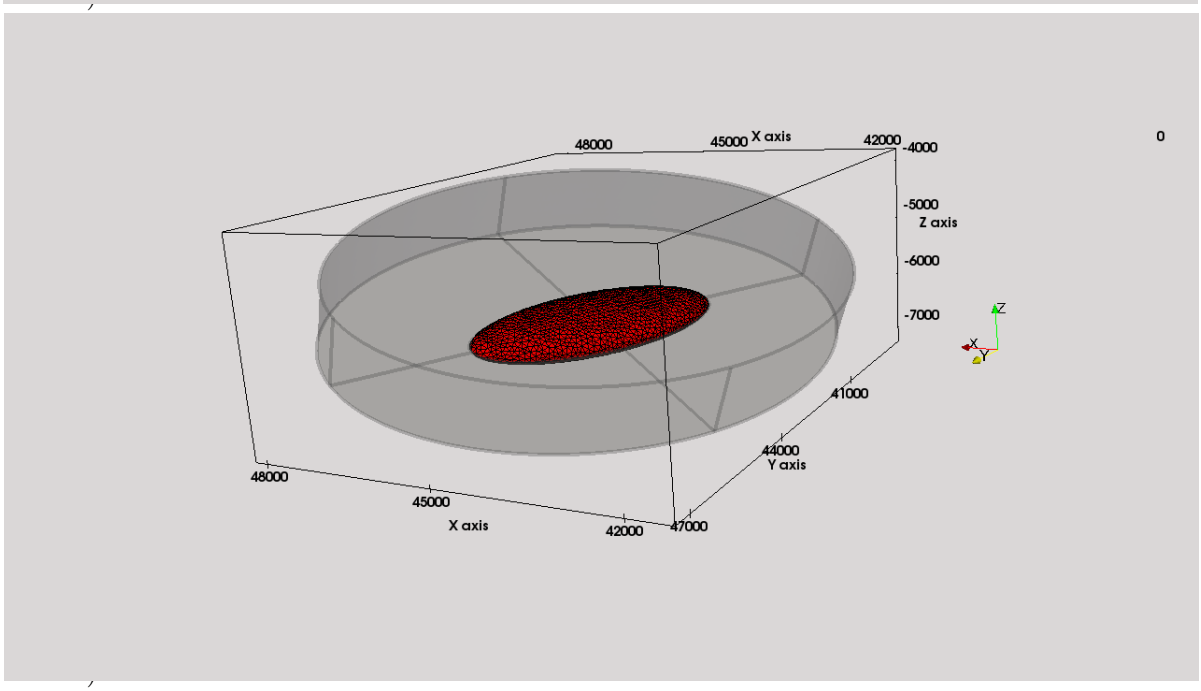

Figure S9: a) A pressurized elliptical source (red) surrounded by an elastic medium. b) a smaller pressurized source (in red), surrounded by an ellipitical source; which represents the viscoelastic shell.

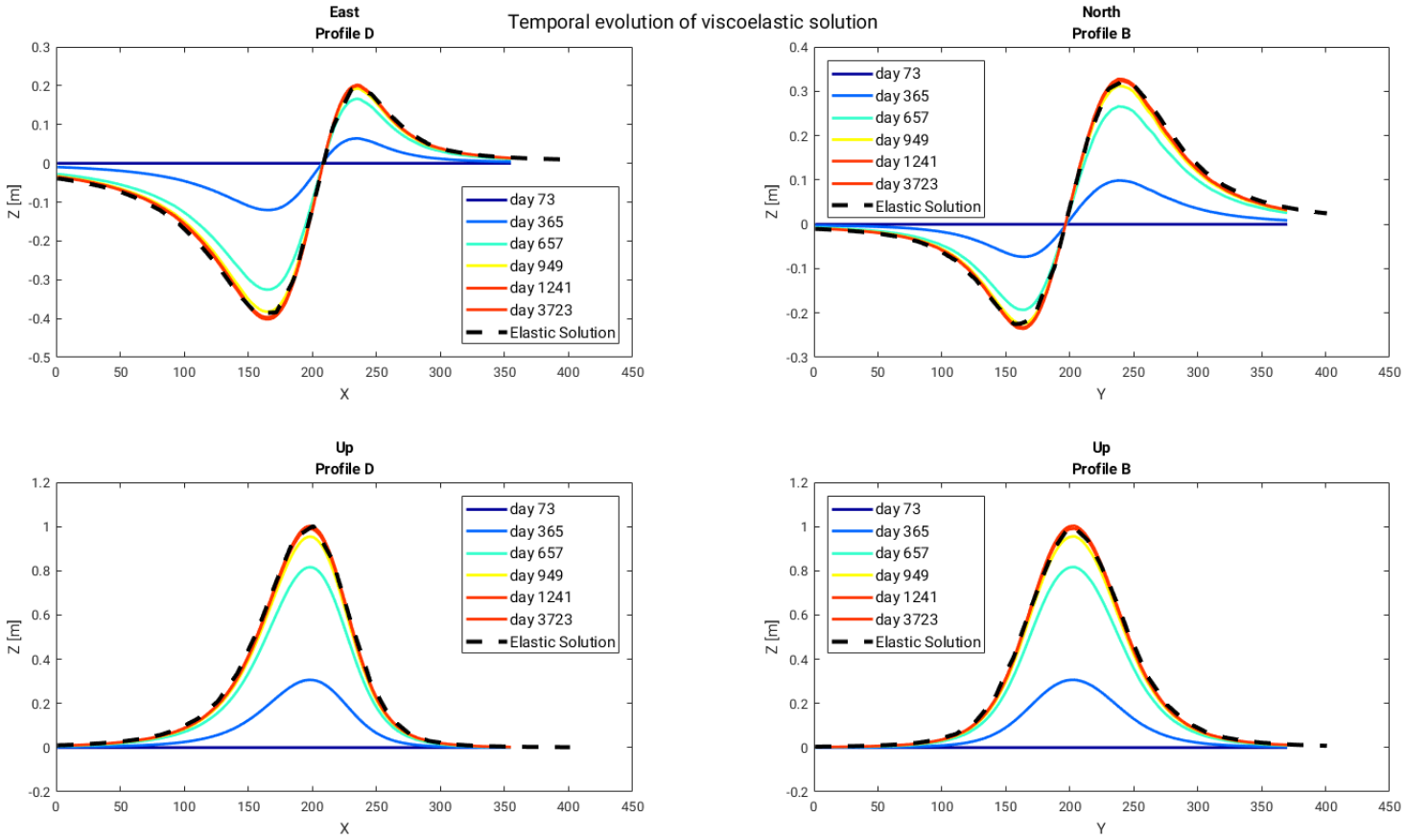

Figure S10: Temporal evolution of surface displacement (east, north and up) along profile B of Fig. S14 and profile D of Fig. S13 produced by the 'Viscoelastic source'. Surface displacements evolve in time (from blue to red) as the pressure is transferred to the shell's wall. When the pressure is completely transferred to the shell's wall the surface displacement remains constant and mimicks the solution of the 'Elastic source'.

a)

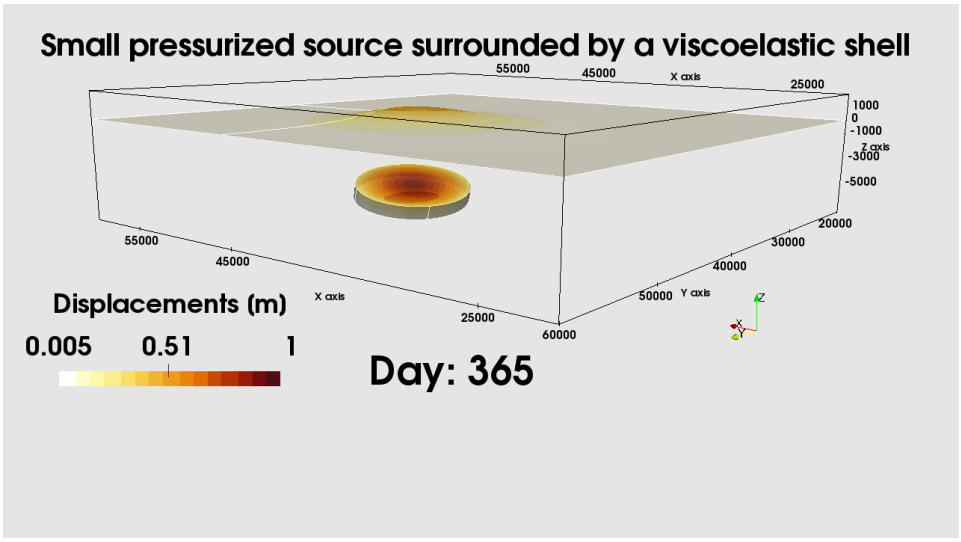

b)

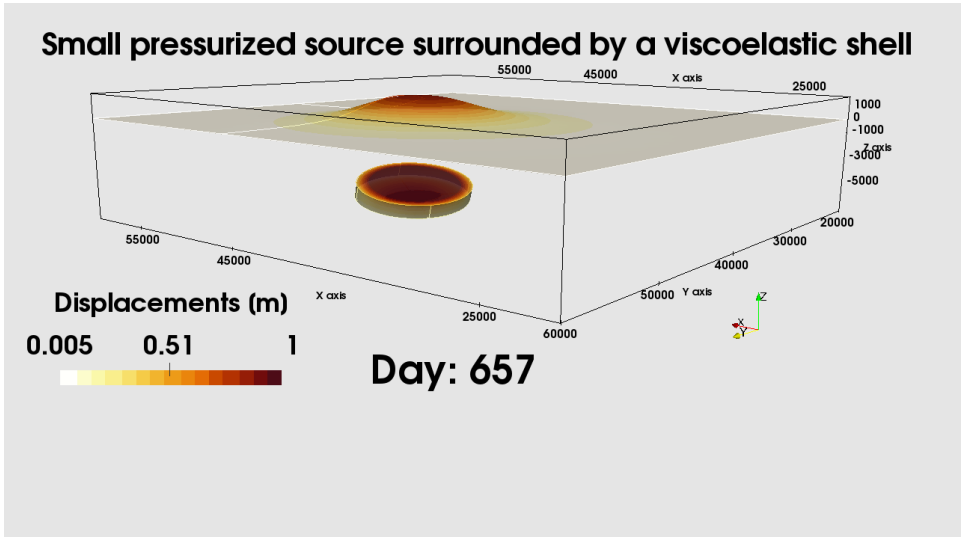

c)

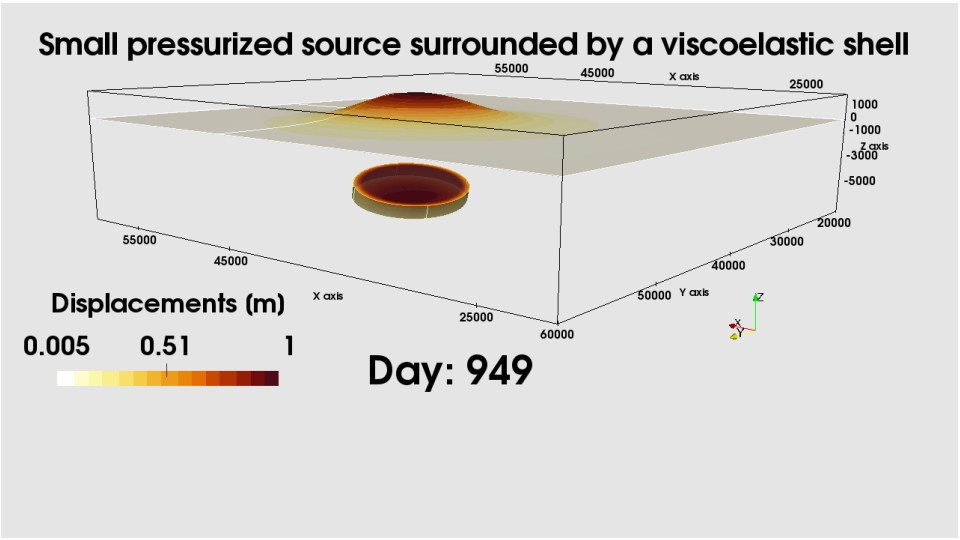

Figure S11: Temporal evolution of surface displacement (magnitud) produced by the 'Viscoelastic source'. The surface displacements evolve in time; from 1 year (365 days) to 949 days. At 949 days the pressure is completely transferred to the shell's wall (in agreement with figure S10).

a)

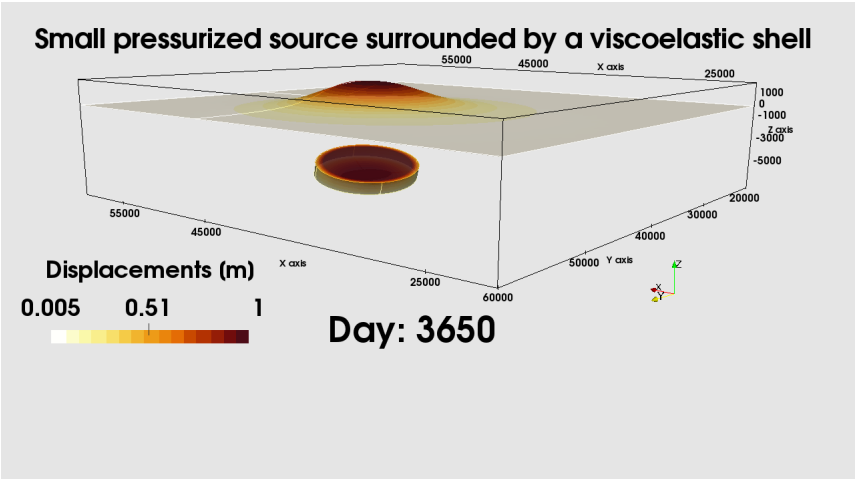

b)

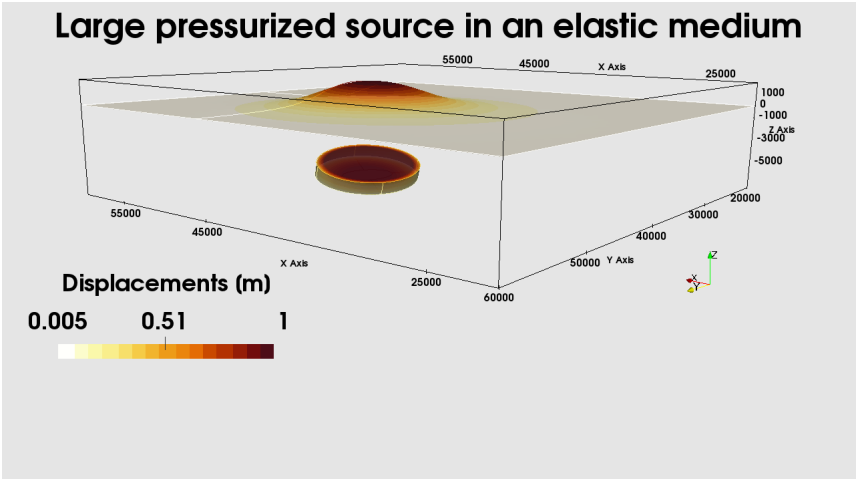

Figure S12: a) Displacements (magnitud) produced by the 'Viscoelastic source' after 10 years (3650 days). b) Displacements (magnitud) produced by the 'Elastic source'. In case (a) the pressure is completely transferred to the shell's walls and mimicks the displacements produced in case (b).

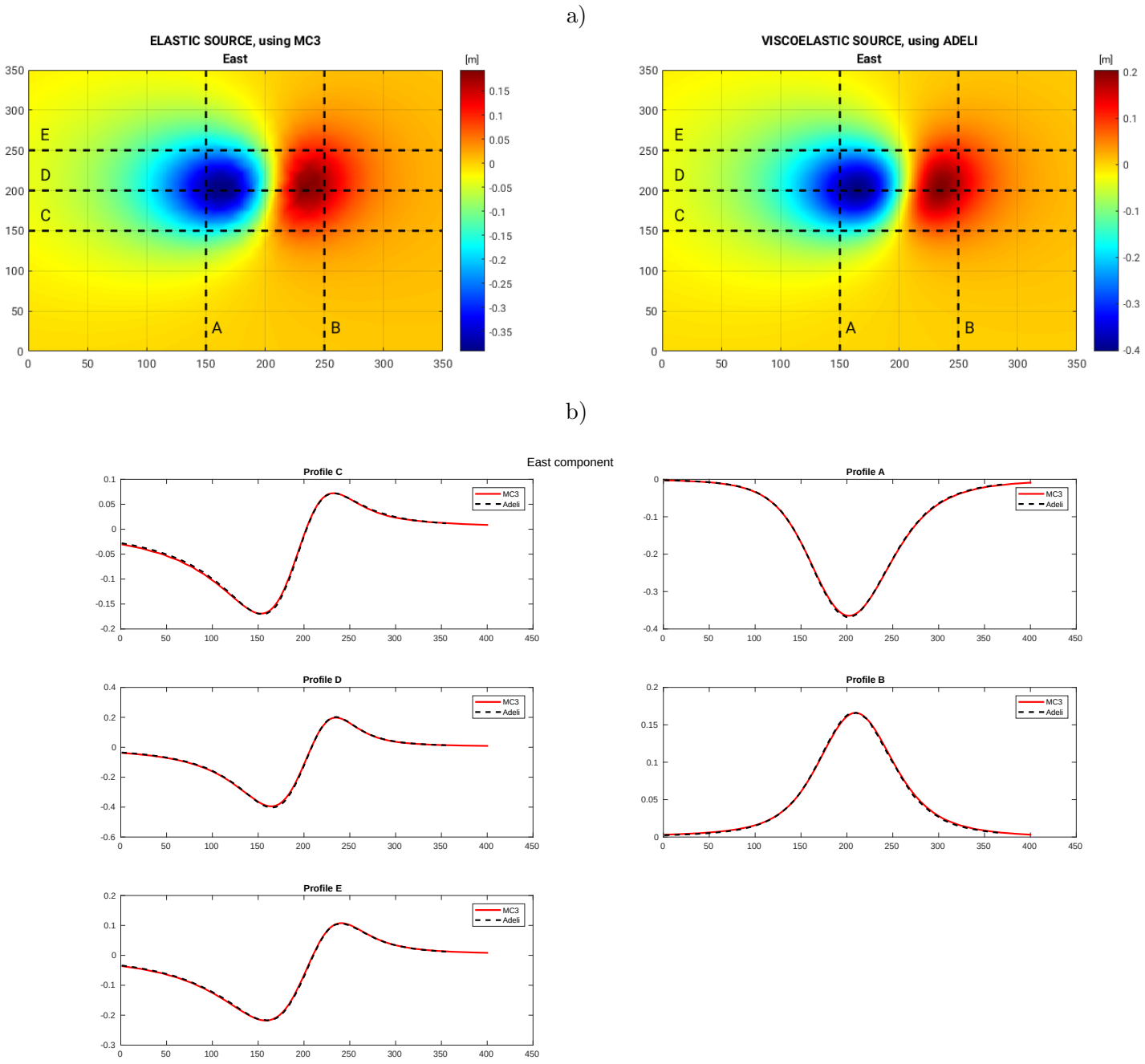

Figure S13: Comparison of the numerical solutions of surface displacements (East component) produced by the 'Elastic source' (left) obtained from a three dimensional boundary element method (MC3, Cayol and Cornet, (1998)) with ADELI's numerical solutions produced by the 'Viscoelastic source' after 10 years (right) along profiles A, B, C, D, and E.

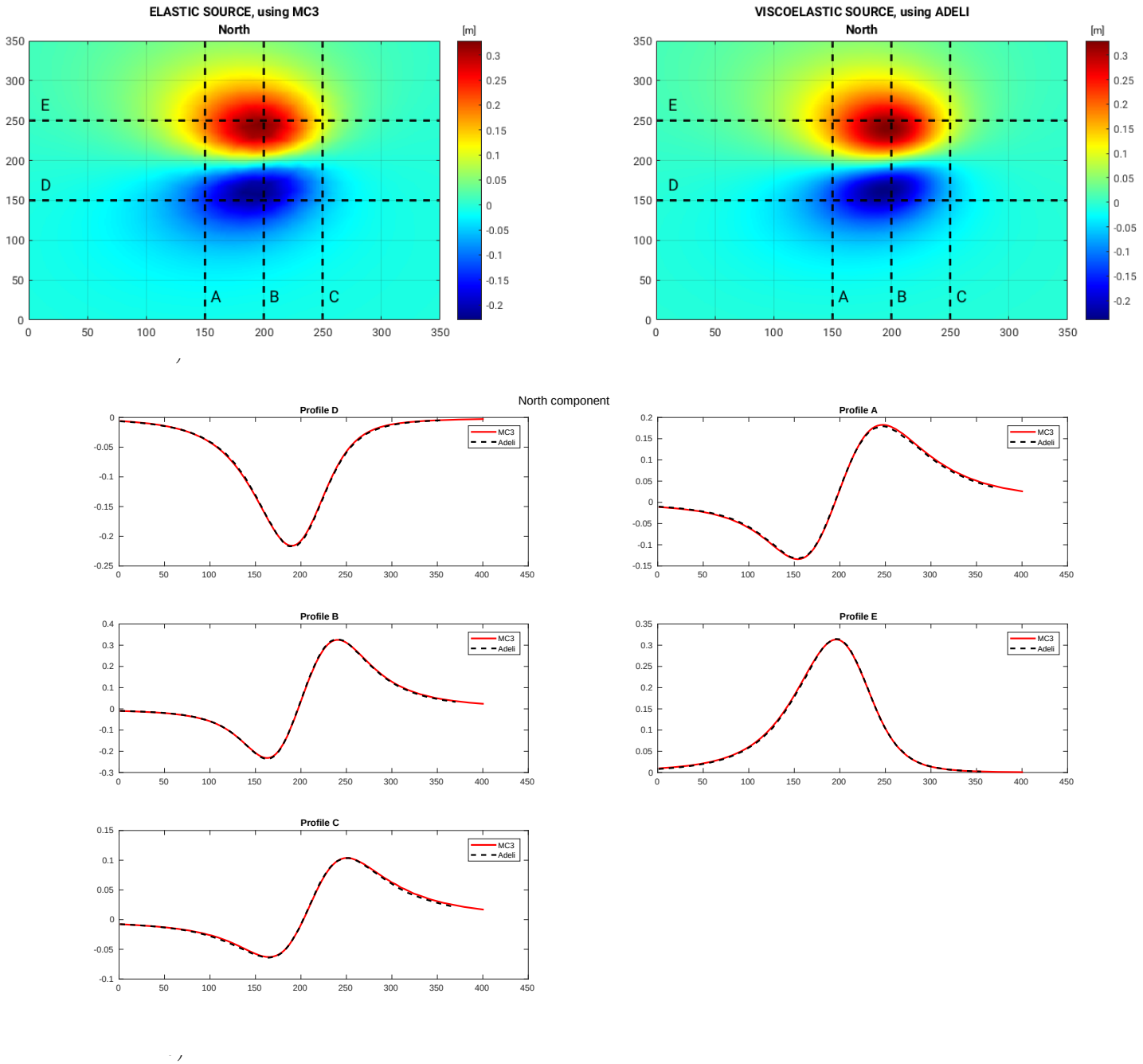

Figure S14: Comparison of the numerical solutions of surface displacements (North component) produced by the 'Elastic source' (left) obtained from a three dimensional boundary element method (MC3, Cayol and Cornet, (1998)) with ADELI's numerical solutions produced by the 'Viscoelastic source' after 10 years (right) along profiles A, B, C, D, and E.

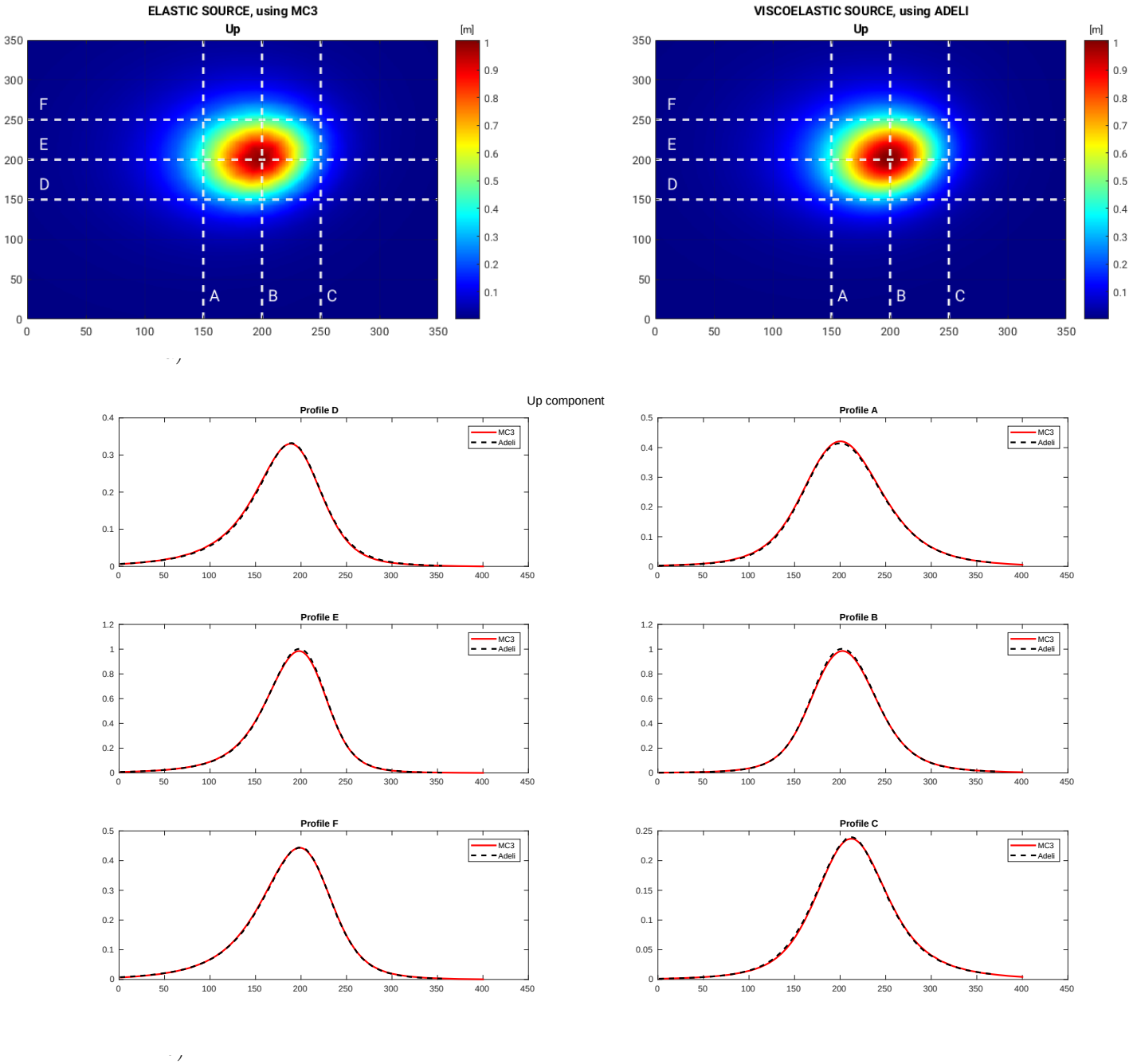

Figure S15: Comparison of the numerical solutions of surface displacements (Up component) produced by the 'Elastic source' (left) obtained from a three dimensional boundary element method (MC3, Cayol and Cornet, (1998)) with ADELI's numerical solutions produced by the 'Viscoelastic source' at 10 years (right) along profiles A, B, C, D, E and F.

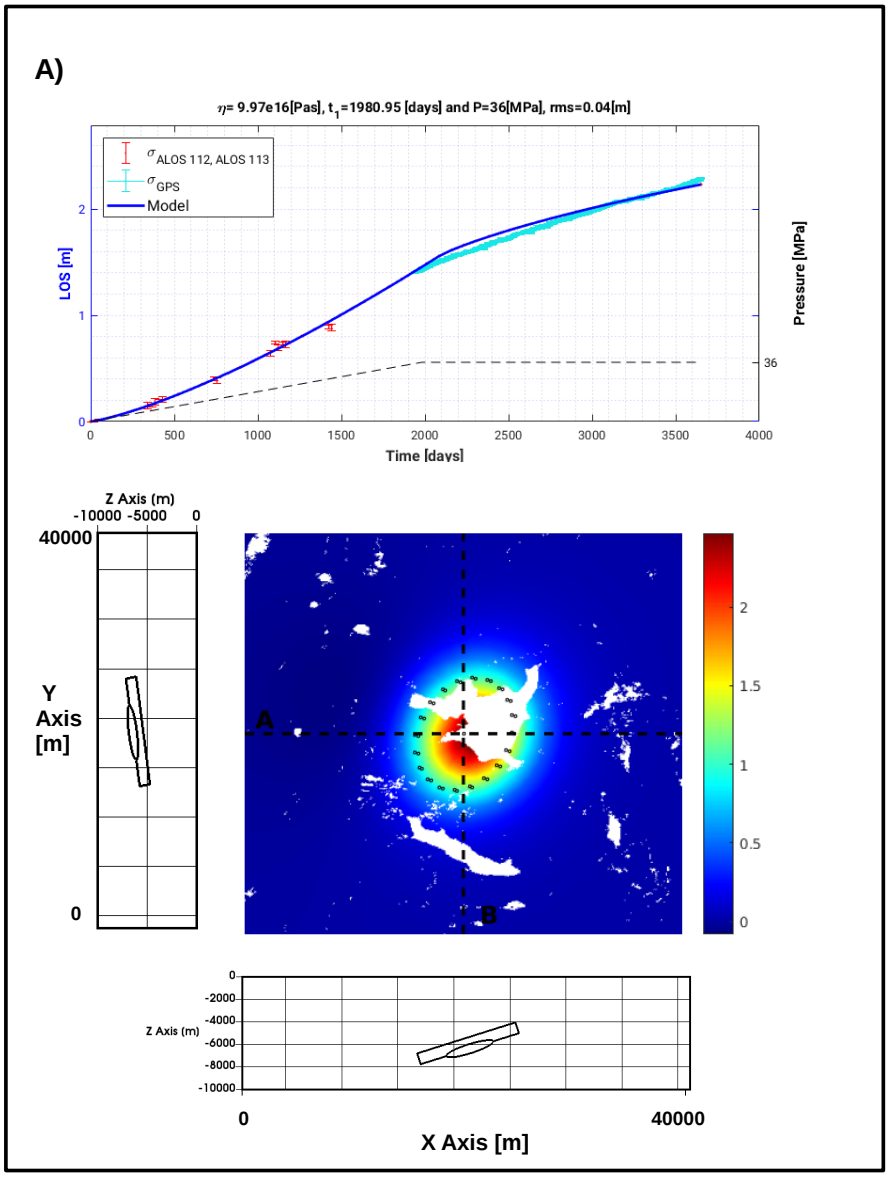

Figure S16: Results of the best fit of the temporal evolution of surface displacements at MAU2 in the last 10 years (3650 days). This figure (A) represents model 1 elliptical truncated cone geometry, used in the main text. The upper panel of each figures provides the parameters associated to the best model η: viscosity, t1: loading time, P: pressure, and rms: root mean square error. The bottom panel includes the map of the modeled surface displacement in 2017 (after 10 years of active surface deformation). The projected geometrical models at depth are included in the east and north axes.

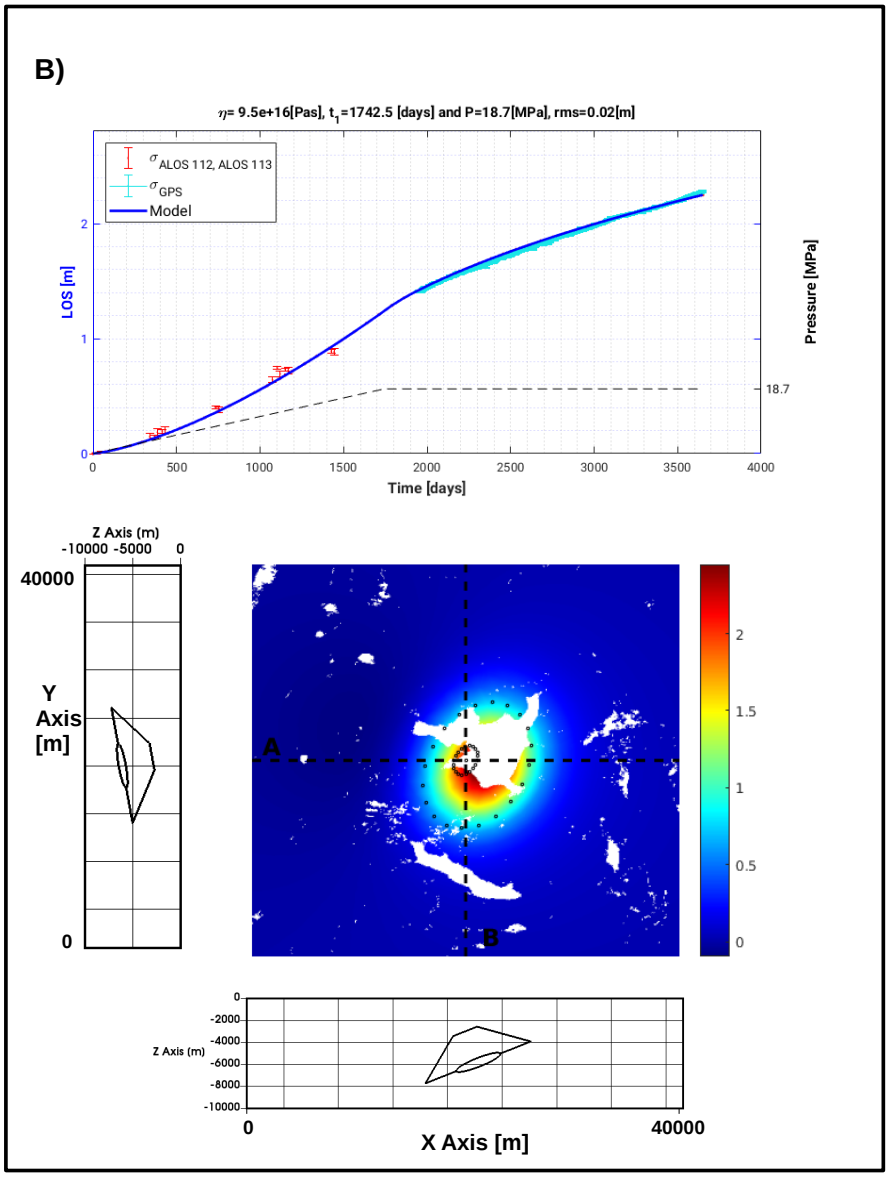

Figure S17: Results of the best fit of the temporal evolution of surface displacements at MAU2 in the last 10 years (3650 days). This figure (B) represent model 2 elliptical truncated cone geometry used in the main text. The upper panel of each figures includes the parameters associated to the best model η: viscosity, t1: loading time, P: pressure, and rms: root mean square error. The bottom panel includes the map of the modeled surface displacement in 2017 (after 10 years of active surface deformation). The projected geometrical models at depth are included in the east and north axes.

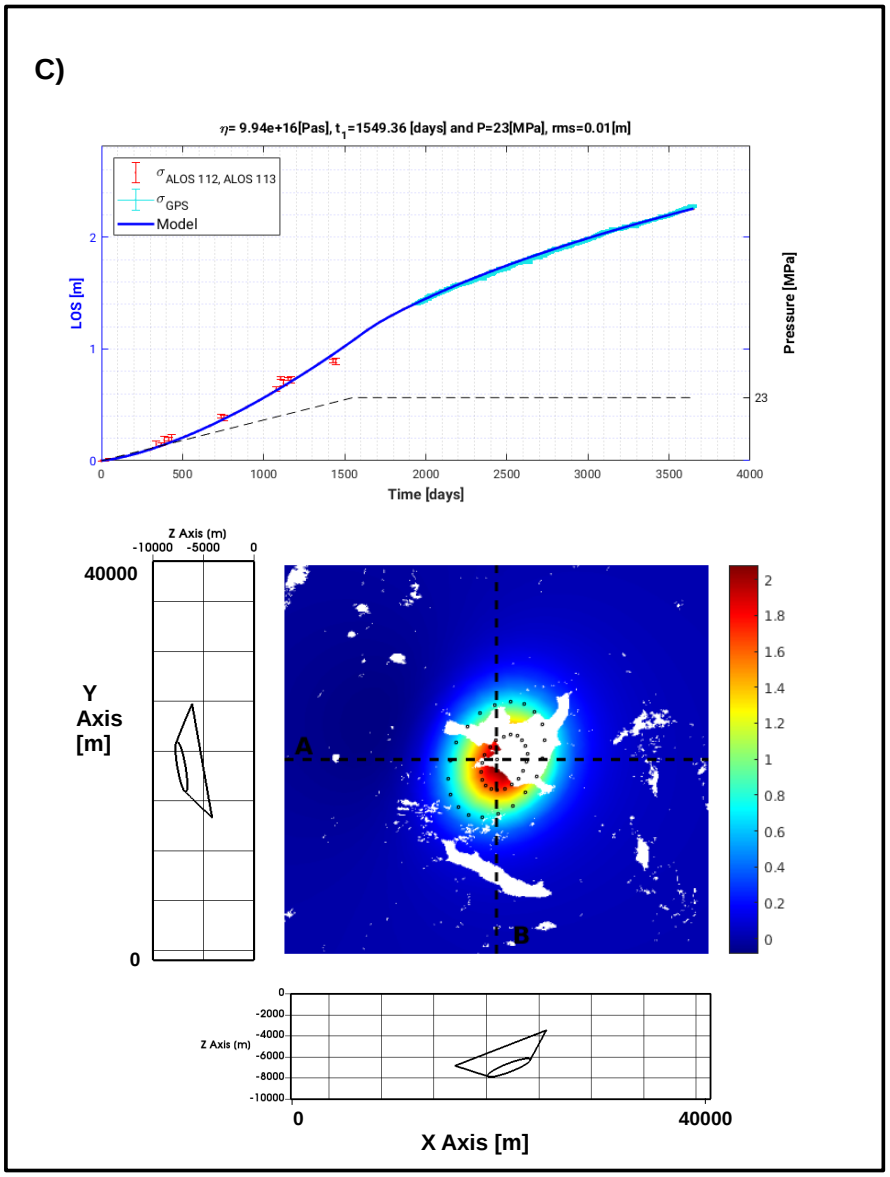

Figure S18: Results of the best fit of the temporal evolution of surface displacements at MAU2 in the last 10 years (3650 days). This figure (C) represent model 3 elliptical truncated cone geometry used in the main text. The upper panel of each figures includes the parameters associated to the best model η: viscosity, t1: loading time, P: pressure, and rms: root mean square error. The bottom panel includes the map of the modeled surface displacement in 2017 (after 10 years of active surface deformation). The projected geometrical models at depth are included in the east and north axes.

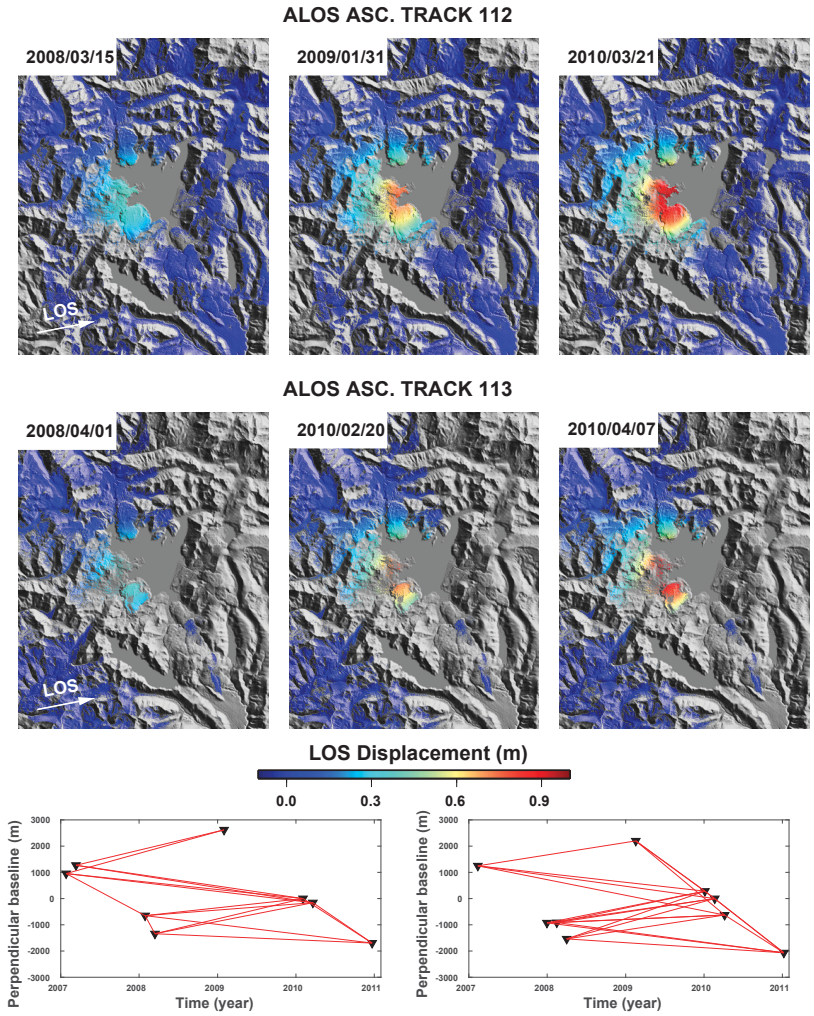

Figure S19: Subset of ALOS-1 interferograms formed with images acquired in ascending mode tracks 112 and 113 overlaid onto a shaded relief map. The lower part represents the perpendicular baseline (in meters) as function of time. Black triangles and red lines represent the SAR images and the interferograms used to extent the period of ground displacement measurements at the location of the GNSS station MAU2. The satellite to ground radar line of sight LOS is shown with a white arrow. LOS displacements toward the satellite are positive. The areas shown in gray indicate areas which are not coherent.

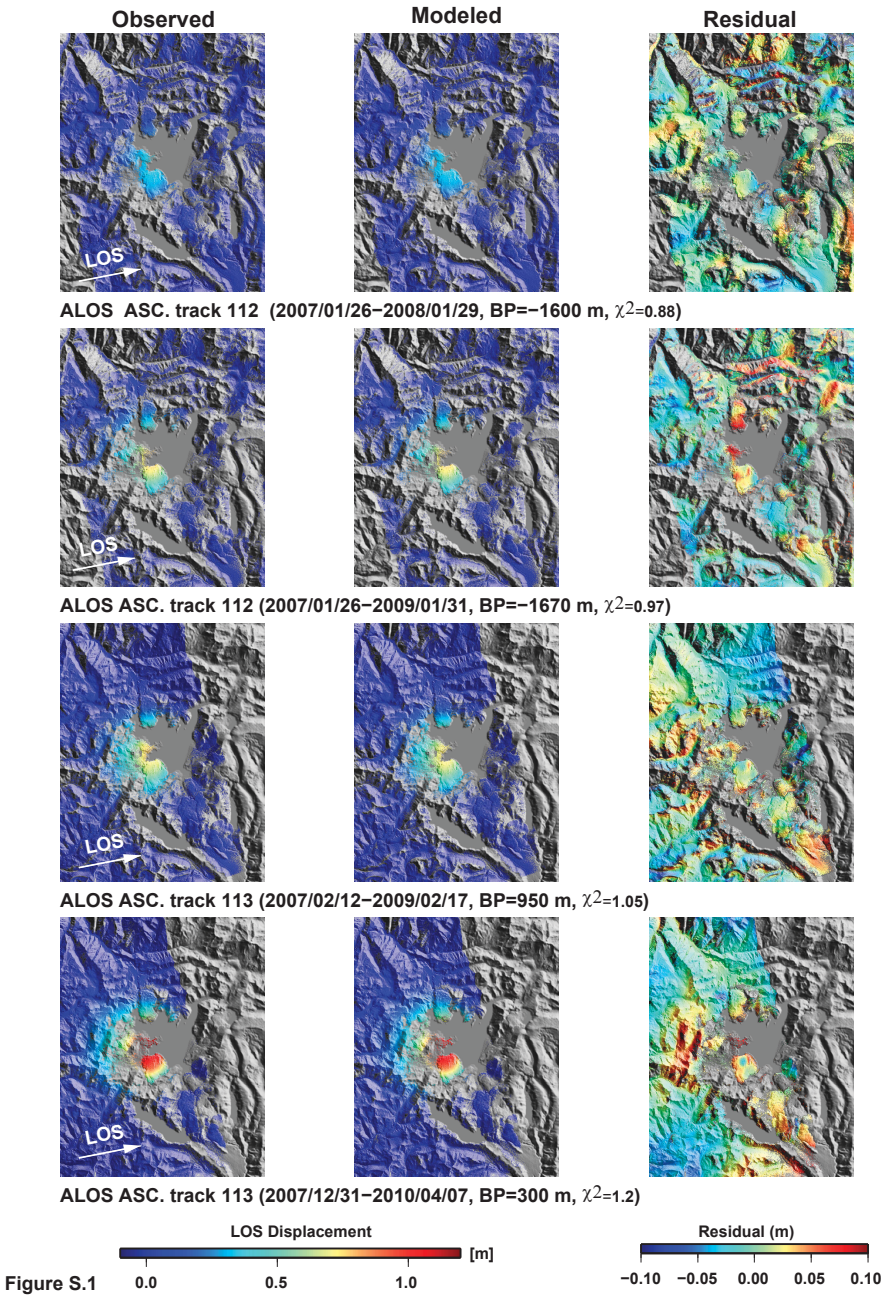

Figure S20: Model predictions for the ground surface displacements observed from 2007 to 2010 by ALOS-1 obtained from the best fit elliptical truncated model (Model 2). The satellite to ground radar line of sight LOS is shown with a black arrow. LOS displacements toward the satellite are positive. The areas shown in gray indicate area which are not coherent.

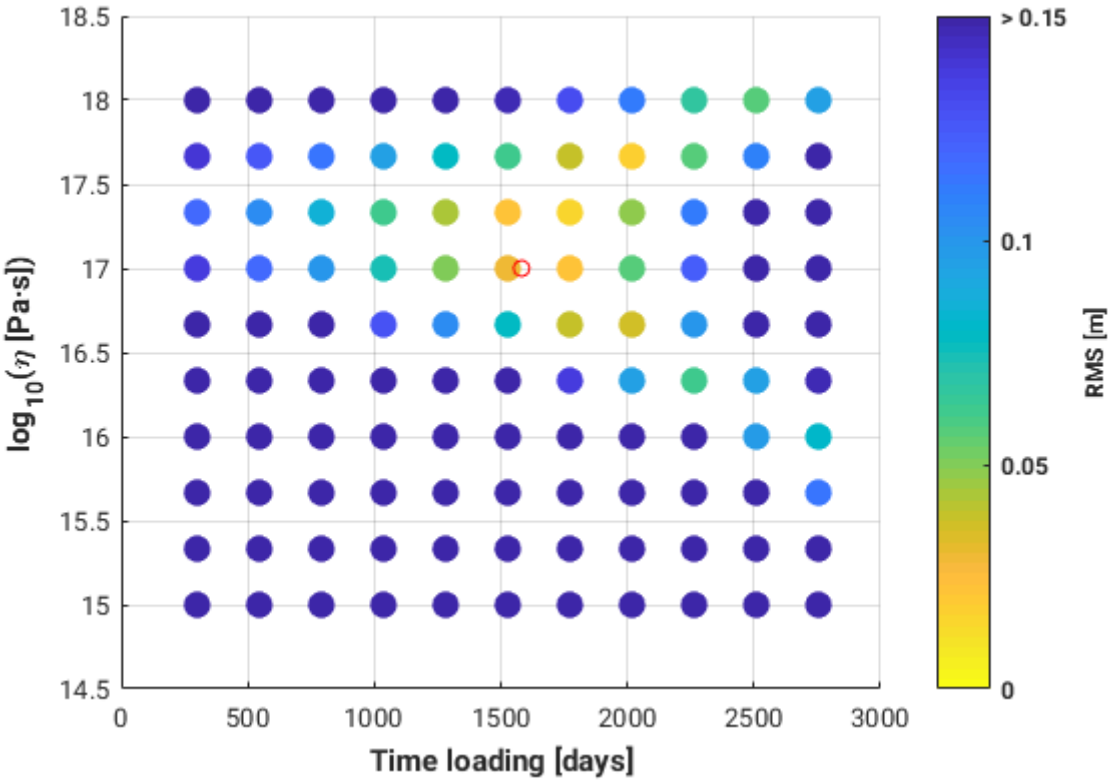

Figure S21: RMS plot of viscosity (η) versus loading time for our best model (model geometry 3, in Figure 7 of the main text). The red circle shows the model used to match the observations.

Model form	Mogi	Yang	Okada
χ_r^2	2.4	2.14	1.08
X position (km)	361.750	362.617	360.270
Y position (km)	6006.983	6007.499	6007.496
Depth (km)	5.16	4.35	6.7
$\nabla V(km^3y^{-1})$	0.02	0.021	0.024
Length	-	6.3	6.9
Width	-	1.95	3.5
Strike (°)	-	76	67
Dip (°)	-	2.49	-21

Table S1: Model predictions from the best fit classical analytical models (Mogi-type point source, spheroidal Yang-type source and Okada-type dislocation). X and Y are expressed in km (UTM WGS84 zone 19 South). Depth is expressed in m below the mean surface elevation (i.e., 2500 m asl). ∇V is the rate of volume change from October, 2014 to July 2017. Length is the length of the rectangle of the Okada-type dislocation and the semimajor axis for the spheroidal Yang-type source. Width is the width of the rectangle of the Okada-type dislocation and the semiminor axis for the spheroidal Yang-type source. Strike is counterclockwise angle relative to the east and Dip is the dip angle.

Pressurized source: R_1	0.5 [km]
Concentric spheric shell:R_2	1.5 [km]
Distance from source center and point of measure: r	6 [km]
Gravity	0
η(viscosity)	10^{16} [Pa s]
Pressure	30 [MPa]
Rigidity (Shear modulus)	5 [GPa]
Poisson ratio	0.25
t_1	200 [days]
t_2	400 [days]
t_3	600 [days]

Table S2: Parameters used in Dragoni's model related to Figure S4

References

[1] Chen, C. W., and H. A. Zebker (2002), Phase unwrapping for large SAR interferograms: Statistical segmentation and generalized network models, IEEE Transactions on Geoscience and Remote Sensing, 40, 1709-1719.

[2] Diapason (2006) Automated interferometric processing software version 4.0, Altamira Information, France

[3] Dragoni M, Magnanensi C (1989) Displacement and stress produced by a pressurized, spherical magma chamber, surrounded by a viscoelastic shell. Phys Earth Planet Int 56:316–328.

[4] Goldstein, R. M., H. A. Zebker, and C. L. Werner (1988), Satelite radar interferometry : two dimensional phase unwrapping, Radio Sciences, 23, 713-720.

[5] Massonnet, D., and K. L. Feigl (1995), Discrimination of geophysical phenomena in satellite radar interferograms, Geophysical Research Letters, 22, 1537-1540.

[6] Newman, A. V., Dixon, T. H., Ofoegbu, G. I., & Dixon, J. E. (2001). Geodetic and seismic constraints on recent activity at Long Valley Caldera, California: evidence for viscoelastic rheology. Journal of Volcanology and Geothermal Research, 105(3), 183-206.

[7] Pascal, K., J. Neuberg, and E. Rivalta (2013), On precisely modelling surface deformation due to interacting magma chambers and dykes, Geophysical Journal International, 196(1), 253-278.

[8] Remy, D., J. L. Froger, H. Perfettini, S. Bonvalot, G. Gabalda, F. Albino, V. Cayol, D. Legrand, and M. D. Saint Blanquat (2014), Persistent uplift of the Lazufre volcanic complex (Central Andes): New insights from PCAIM inversion of InSAR time series and GPS data, Geochemistry, Geophysics, Geosystems, 15(9), 3591-3611.

[9] Segall, P. (2010). Earthquake and volcano deformation. Princeton University Press.

[10] Wright, T., B. Parson, and L. Zhong (2004). Toward mapping surface deformation in three dimension using InSAR, Geophysical Research Letters, doi:10.1029/2003GL018827.